Nano Research

Open Access

Research Article

Nanoscale platelet extracellular vesicles mediate inflammatory lung injury through Cd36–Fyn-dependent macrophage polarization in transfusion-related acute lung injury

Chenggao Wu[1,§], Jiamei Hu[2,§], Wei Liu[1], Linju Kuang[1], Yize Wu[1], and Aiping Le[1]

[1] *Department of Transfusion Medicine, Key Laboratory of Jiangxi Province for Transfusion Medicine, The First Affiliated Hospital, Jiangxi Medical College, Nanchang University, Nanchang 330006, China*
[2] *The Center of Breast Professional Disease Diagnosis and Treatment, The First Affiliated Hospital, Jiangxi Medical College, Nanchang University, Nanchang 330006, China*
[§] *Chenggao Wu and Jiamei Hu contributed equally to this work.*

Cite this article: *Nano Research*, **2026**, *19*, 94908388. https://doi.org/10.26599/NR.2026.94908388

ABSTRACT: Platelet-derived extracellular vesicles (pEVs) are abundant nanoscale bioeffectors released during platelet storage, yet their functional roles in transfusion-associated complications remain largely unexplored. The present study demonstrates that pEVs act as potent nanocarriers that aggravate transfusion-related acute lung injury (TRALI) through activation of the Cd36–Fyn signaling pathway in macrophages. Integrated single-cell RNA sequencing and mechanistic analyses demonstrated that pEVs administration selectively induced M1 macrophage polarization and amplified pulmonary inflammation. Cd36 was markedly upregulated in the Fn1^{+} macrophage subset, serving as the receptor that mediates pEV uptake and Fyn activation. Molecular and pharmacological inhibition of Cd36–Fyn signaling significantly attenuated pro-inflammatory cytokine expression, lung tissue damage, and mortality *in vivo*. These findings elucidate how nanoscale platelet vesicles reprogram macrophage responses and disrupt immune homeostasis, providing a mechanistic framework for understanding TRALI progression. Identification of the Cd36–Fyn axis as a molecular link between nanovesicle signaling and immune dysregulation highlights new therapeutic opportunities for transfusion safety and nanomedicine-based interventions.

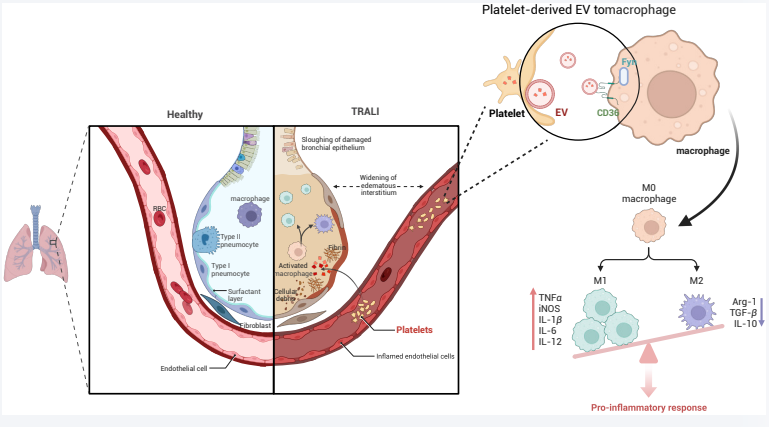

KEYWORDS: transfusion-related acute lung injury, platelet-derived extracellular vesicles, M1 macrophages, Cd36–Fyn pathway, therapeutic strategy

1 Introduction

Blood transfusion represents an essential therapeutic intervention in various clinical conditions and surgical procedures. Despite its widespread use, transfusion-related acute lung injury (TRALI) remains one of the most severe and life-threatening transfusion complications, markedly increasing patient mortality and prolonging hospital stay [1–3]. TRALI typically occurs during or within six hours after transfusion and is characterized by acute hypoxemia and non-cardiogenic pulmonary edema. Although extensive research has been conducted, the pathogenic mechanisms underlying TRALI remain incompletely understood [4, 5]. TRALI represents a global health concern, with incidence rates varying markedly across patient populations, occurring in approximately one case per 10,000 transfusions in the general population but exceeding one case per 100 transfusions among critically ill patients [6]. Since the first description of TRALI in 1957, understanding of its underlying mechanisms has progressively advanced. In 1983,

Received: October 7, 2025; **Revised:** December 26, 2025
Accepted: December 30, 2025

✉Address correspondence to ndyfy00973@ncu.edu.cn

TRALI was formally recognized as a clinical syndrome primarily mediated by antibodies against human leukocyte antigens [7]. Additionally, antibodies against human neutrophil antigens, soluble CD40 ligands, and lysophosphatidylcholine have also been shown to induce TRALI [8, 9]. More recent evidence indicates that prolonged platelet storage results in the release of substantial amounts of bioactive regulatory factors and platelet-derived extracellular vesicles (pEVs), which induce characteristic TRALI pathological features in lipopolysaccharide (LPS)-sensitized mice [6].

Although donor management, blood component optimization, and patient blood management strategies have reduced the overall incidence of TRALI, targeted therapeutic options remain unavailable, and clinical management relies largely on supportive care. Therefore, further elucidation of the immune mechanisms underlying TRALI and identifying novel therapeutic targets are essential for improving prognosis and developing individualized treatment strategies.

Extracellular vesicles (EVs) are membrane-bound particles released by diverse cell types and serve critical functions in intercellular communication, immune regulation, and tissue homeostasis [10–12]. Increasing evidence indicates that pEVs possess substantial pathogenic potential in pulmonary disorders. In models of acute respiratory distress syndrome and acute lung injury, pEVs aggravate pulmonary inflammation by promoting endothelial dysfunction and immune cell activation. Clinical studies have further reported markedly elevated pEV levels in patients with COVID-19, supporting a role for pEVs in virus-associated lung injury [13]. Notably, pEVs have been widely reported to be closely associated with the onset of TRALI [14], although the underlying molecular mechanisms remain to be fully elucidated.

M1 macrophage polarization represents a central mechanism driving acute pulmonary inflammatory responses. Through the production of pro-inflammatory mediators, including tumor necrosis factor-alpha (TNF-α), interleukin-6 (IL-6), and inducible nitric oxide synthase (iNOS), M1 macrophages establish an inflammatory microenvironment that contributes to TRALI progression [15, 16]. Multiple studies have indicated that EVs can regulate macrophage polarization via miRNAs, lipids, and proteins [17–19]. However, whether pEVs aggravate TRALI by inducing M1 polarization through specific signaling axes has not been fully elucidated.

CD36 (also known as fatty acid transferase (FAT), glycoprotein IIIb (GPIIIb), or glycoprotein IV (GPIV)) is a class II scavenger receptor widely expressed in macrophages, endothelial cells, hepatocytes, cardiomyocytes, and platelets [20]. CD36 mediates the recognition and internalization of diverse ligands, including oxidized lipids, phospholipids, and advanced glycation end products [21, 22]. Beyond its involvement in TRALI, CD36 contributes to the pathogenesis of multiple inflammatory disorders, such as atherosclerosis, diabetic nephropathy, and nonalcoholic steatohepatitis (NASH), where activation of the downstream Fyn signaling pathway drives M1 macrophage polarization [23]. Cd36–Fyn may represent a shared immunoregulatory axis across various inflammatory conditions. Whether platelet-derived extracellular vesicles induce M1 polarization and promote the initiation or progression of TRALI through activation of the CD36–Fyn signaling pathway has not yet been systematically examined.

Based on this background, this study aimed to establish a TRALI mouse model induced by LPS combined with pEVs and to analyze the dynamic changes of macrophage subpopulations in lung tissue using single-cell RNA sequencing (scRNA-seq), with particular emphasis on M1 polarization and the expression profiles of its key regulatory factors Cd36 and Fyn. Complementary *in vitro* pEV stimulation, gene interference, functional inhibition, and conditional knockout mouse approaches were employed to systematically determine whether the Cd36–Fyn pathway serves a central role in pEVs-mediated M1 macrophage polarization and TRALI pathogenesis.

This study aimed to elucidate how pEVs-mediated Cd36–Fyn signaling drives M1 macrophage polarization and thereby promotes the pathological progression of TRALI. The findings are expected to provide a theoretical and experimental basis for targeted TRALI intervention and offer potential insights into immunotherapeutic strategies for related inflammatory lung injuries.

2 Experimental

2.1 Ethical statement

All animal experiments were conducted in strict accordance with established ethical guidelines and regulatory requirements. The animal study protocol was approved by the Institutional Animal Care and Use Committee at The First Affiliated Hospital of Nanchang University. Animals were maintained under humane conditions, and all procedures were performed with efforts to minimize pain and distress. At the completion of the experiments, mice were euthanized under anesthesia using 0.3% pentobarbital sodium.

2.2 Platelet extraction and EVs purification

Whole blood was collected from wild-type BALB/c mice (female, 6–7 weeks of age, body weight 16–18 g; Beijing Vital River Laboratory Animal Technology Co., Ltd.). Platelet-rich plasma (PRP) was prepared by three sequential centrifugations of whole blood at 200*g* for 15 min at room temperature. The resulting plasma was centrifuged at 1000*g* for 18 min at room temperature, and the pellets were pooled. Platelets were stored in a sterile biosafety cabinet with gentle agitation on a horizontally oriented orbital shaker, as previously described [24]. Storage durations included 1, 3, and 5 days (D1, D3, and D5). Approximately 1×10^9 platelets were used per mouse for pEV isolation. EVs were isolated from platelets using differential centrifugation. Platelets stored for different durations were centrifuged at 4 °C and 2000*g* for 30 min to remove intact platelets and cellular debris, and the supernatant was collected. The supernatant was then centrifuged at 4 °C and 10,000*g* for 30 min to eliminate larger particles and organelles, and the resulting supernatant was retained. The resulting supernatant was centrifuged at 5000*g* for 2 h at 4 °C to separate primary platelet microparticles (pellet) and microparticle-free supernatant. The pellet was resuspended in 1 mL phosphate-buffered saline (PBS), passed through a 0.1 μm pore-size filter to remove any residual large particles, and then centrifuged at 5000*g* for 2 h at 4 °C to obtain further purified vesicular microparticles, defined as pEVs. The pEVs were finally resuspended in 300 μL PBS and stored at −80 °C for subsequent analyses.

2.3 Nanoparticle tracking analysis (NTA)

The concentration and size distribution of pEVs were analyzed

using a NanoSight LM10 nanoparticle tracking analyzer (Malvern, UK). Samples were manually loaded, and measurements were conducted at room temperature. Supernatants were analyzed either without dilution or after serial dilution (1:2, 1:10, 1:20, or 1:100) in 0.1 μm-filtered Tyrode-HEPES buffer to achieve an optimal particle concentration (1×10^6–1×10^9 particles/mL). Each sample was measured in duplicate. The acquired data were further analyzed using NTA software version 2.2.

2.4 Transmission electron microscopy (TEM)

Supernatants containing total EVs were deposited onto 200-mesh copper grids coated with Pioloform and carbon film and subjected to glow discharge (Agar Scientific, UK). After incubation for 60 s, the grids were air-dried at room temperature and negatively stained with 3% (w/v) aqueous uranyl acetate (System Biosciences, USA) for 20 s. Imaging was performed at an accelerating voltage of 120 kV using a Gatan Multiscan 794 (1 × 1 k) charge-coupled device (CCD) camera mounted on a Tecnai 12 transmission electron microscope (FEI, Netherlands). For each experimental condition, vesicle diameters were manually measured for at least 400 individual particles.

2.5 Protein quantification

The total protein content of the pEV pellets was determined using the Micro BCA Protein Assay Kit (A65453, Thermo Scientific, USA), with bovine serum albumin (BSA) as the standard. Pellets were resuspended in PBS containing 0.25% Triton X-100 (T8787, Sigma-Aldrich, Germany). Samples and standards were mixed with the working reagent and incubated at 37 °C for 2 h. Absorbance was recorded at 560 nm using a Multiscan EX microplate reader (Thermo Scientific, USA).

2.6 Detection of platelet metabolic and activation markers

Based on previous research [25], platelet lactate (LA) levels and pH were measured using a blood gas analyzer (Radiometer, Denmark). Lactate dehydrogenase (LDH) activity was assessed with an automated biochemical analyzer (Beckman Coulter, USA). Platelet activation was evaluated by measuring surface expression of CD62P using flow cytometry. Platelet suspensions were adjusted to 2×10^{11}/L, and 5 μL aliquots were stained with anti-CD62P antibody for analysis of CD62P expression on the platelet surface.

2.7 pEVs-induced two-hit transfusion-related acute lung injury (TRALI) mouse model

Wild-type BALB/c mice were intraperitoneally injected with LPS (5 mg/kg; L5293, Sigma-Aldrich LLC, Merck KGaA, Darmstadt, Germany). Two hours later, mice received an intraperitoneal injection of pEVs suspension (0.5 mL/kg), corresponding to the amount of EVs (platelet-free) present in 0.5 mL/kg of platelet concentrates derived from platelets stored for different durations (D1 or D5) to establish a pEVs-induced two-hit TRALI mouse model [6]. An equal volume of PBS served as a negative control. In additional groups, mice were treated with LPS followed by intravenous anti-Cd36 antibody (1 μg/mL; NB600-1423, Bio-Techne China), either alone or combined with intraperitoneal administration of the tyrosine kinase inhibitor PP2 (10 mg; 1407, R&D Systems). Two hours later, pEVs suspension (0.5 mL/kg) was administered intraperitoneally. The experimental groups included PBS, LPS (5 mg/kg), LPS + platelet, LPS + pEVs (D1 or D5), LPS + pEVs (TRALI) + IgG, TRALI + anti-Cd36, TRALI + PP2, and TRALI + anti-Cd36 + PP2. Survival analysis included 10 mice per group, and all other analyses included 5 mice per group. At 24 h after treatment, mice were euthanized under general anesthesia. Bronchoalveolar lavage was performed on the left lung for total protein quantification. The right lung was used for semiquantitative lung injury scoring (upper lobe), cytokine measurement by enzyme-linked immunosorbent assay (ELISA) (middle lobe), and lung wet-to-dry weight ratio analysis (lower lobe) [6].

2.8 Generation of conditional knockout mice

$Cd36^{fl/fl}$ and $Fyn^{fl/fl}$ mice and Cre mice (provided by Biocytogen Co., Ltd.) were housed and bred in laminar flow racks within the animal facility. All procedures complied with national regulations for laboratory animal care and standard operating protocols. $Cd36^{fl/fl}$ mice were crossed with monocyte/macrophage-specific Cre-expressing mice to generate $Cd36^{fl/fl}$ Lyz-Cre mice. These mice were then intercrossed with Cd36-floxed mice carrying a single Cre allele to obtain monocyte/macrophage-specific Cd36 conditional knockout mice. Fyn conditional knockout mice were generated using an identical breeding strategy. TRALI was induced in conditional knockout mice using pEVs according to the established protocol. Experimental groups included: WT + PBS, WT + TRALI, $Cd36^{-/-}$ + TRALI, and $Fyn^{-/-}$ + TRALI. Survival analysis was performed using 10 mice per group, whereas all other analyses included 5 mice per group.

2.9 Assessment of pulmonary edema

Pulmonary edema was quantified using the lung wet-to-dry weight ratio. Mice were anesthetized, and rapid exsanguination was achieved by transection of the abdominal aorta and inferior vena cava. Lungs were excised in full, snap-frozen in liquid nitrogen, and weighed to obtain wet weight. Samples were subsequently lyophilized for 24 h and reweighed to determine dry weight. Lung water content was calculated from the difference between wet and dry weights, and the percentage of tissue water content was determined relative to the pre-drying weight.

2.10 Bronchoalveolar lavage (BAL) and protein quantification

Following anesthesia, the mice were decapitated, and the trachea was exposed and isolated. A small incision was made in the trachea, and a polyethylene catheter (0.97 mm diameter) was inserted. The lungs were flushed three times with 1 mL of Hank's Balanced Salt Solution (H6648, Merck, Darmstadt, Germany) containing 0.02% ethylenediaminetetraacetic acid (EDTA) and ethylene glycol tetraacetic acid (EGTA), without Ca^{2+} and Mg^{2+}. Collected bronchoalveolar lavage fluid was centrifuged at 1200× *g* for 5 min at 4 °C to remove cellular components. The cell-free supernatant was stored at −80 °C. Protein concentration in the Bronchoalveolar lavage fluid (BALF) was measured using the Pierce BCA Protein Assay Kit (23227, Thermo Fisher Scientific, USA), with BSA used as the standard.

2.11 Assessment of hypoxemia

PO_2 levels were measured using the immunoradiometric assay (IRMA) blood gas analyzer (RNA Medical, Devens, MA, USA). Blood samples were obtained by cardiac puncture.

2.12 Evaluation of lung injury

Following thoracotomy, right lung tissues were harvested and fixed

in 4% paraformaldehyde (PFA), followed by dehydration, clearing, paraffin infiltration, and embedding. Tissue sections were prepared and stained with hematoxylin and eosin (H&E). Histopathological evaluation was performed independently by two investigators in a blinded manner. Lung injury severity was quantified using a standardized semiquantitative histological scoring system.

2.13 Flow cytometry analysis

Flow cytometry was performed to characterize M1 and M2 macrophage phenotypes. RAW264.7 macrophages from different treatment groups were collected and resuspended in PBS. For lung tissue analysis, mouse lungs were rinsed three times with cold sterile PBS and minced into small fragments. Tissue digestion was carried out in RPMI 1640 medium supplemented with collagenase type IV (1 mg/mL, 17104019, Gibco, USA) and DNase I (0.1 mg/mL, 18047019, Invitrogen™, USA) at 37 °C for 40 min at 200*g*. The resulting suspension was filtered through a 70 μm nylon mesh and centrifuged at 500*g* for 5 min. Mononuclear cells were enriched using a discontinuous Percoll gradient (50%, 45%, 35%, and 30%), and cells at the 35%–45% interface were collected. Macrophage phenotypes were analyzed using antibodies against F4/80, CD86, and CD206. Cells were fixed overnight in 1% PFA and analyzed the following day using an LSRFortessa™ cell analyzer (BD Biosciences). Data were processed with FlowJo software (Ashland). Detailed antibody information is provided in Table S1 in the Electronic Supplementary Material (ESM).

2.14 ELISA assay

Levels of IL-6, IL-10, and IL-12 in cell culture supernatants or mouse BALF were measured using ELISA kits. The kits included IL-6 (PI326), IL-10 (PI522), and IL-12 (PI530) from Beyotime (Shanghai, China). All measurements were performed in triplicate, and sample collection was conducted in a blinded manner. Absorbance at 450 nm was measured using a multimode microplate reader (Synergy 2, BioTek, USA). Standard curves were generated from serial dilutions, with regression coefficients exceeding 0.99. Cytokine concentrations were calculated from standard curve equations. Detection and quantification limits were determined to confirm assay sensitivity, and statistical analyses were applied to assess intergroup differences while accounting for potential confounding factors.

2.15 *In vivo* tracking of pEVs

Dil-labeled pEVs (0.5 mL/kg) were resuspended in 200 μL PBS buffer and administered intraperitoneally (i.p.) into mice. After 24 h, the lungs, liver, and kidneys were harvested for *ex vivo* evaluation. The biodistribution of Dil-pEVs in the lungs was monitored using the *in vivo* imaging system (IVIS) Spectrum (PerkinElmer, Waltham, MA, USA). Imaging was performed using filters allowing excitation at 560 nm and emission collection at 590 nm to acquire optimal fluorescence signals.

2.16 scRNA-seq analysis

Following cardiac perfusion of control and pEVs-induced transfusion-related acute lung injury mice until lung blanching was observed, lung tissues were collected and finely minced. Tissue dissociation was performed using the Mouse Lung Dissociation Kit (130-095-927, Miltenyi Biotec, Bergisch Gladbach, Germany). Lung immune cells were isolated through sequential filtration, density gradient centrifugation, and red blood cell lysis. $CD11b^+$ immune cells were further isolated using mouse $CD11b^+$ MicroBeads (130-049-601, Miltenyi Biotec, Bergisch Gladbach, Germany). A single-cell suspension was used to construct a mouse lung $CD11b^+$ mononuclear cell transcriptome library using the 10× genomics chromium system, followed by sequencing. Data were analyzed using the R package "Seurat". Quality control was performed to exclude low-quality cells and potential doublets. Unique molecular identifier (UMI) counts were normalized to correct for sequencing depth variation, and highly variable genes were selected for downstream analyses.

2.17 T-distributed stochastic neighbor embedding (t-SNE) clustering analysis

Dimensionality reduction was performed by principal component analysis (PCA) using the top 2000 highly variable genes ranked by variance. The first 17 principal components (PCs) were selected based on the ElbowPlot method in Seurat for subsequent clustering. Cell clusters were identified using the FindClusters function with a resolution parameter of 0.5. Subsequently, the t-SNE algorithm was applied for the nonlinear dimensionality reduction of the scRNA-seq data. Marker genes for each cell subset were identified using functions provided by Seurat. Cell type annotation was further refined using the "SingleR" package, and pseudotime trajectory analysis was performed with the monocle package.

2.18 RNA-Seq

BALF samples were collected from four mice in the normal control group and four mice in the pEVs-induced TRALI group. Samples were stained with antibodies, and macrophages were sorted using a cell sorter for RNA-Seq analysis (Illumina HiSeq). Sequencing libraries were prepared using the NEBNext® Ultra™ RNA Library Prep Kit for Illumina® (E7530, NEB, Beverly, MA). Quality control was performed using RNA-SeQC v1.1.8 and read counting was conducted using HTSeq-counts v0.7.2. Differentially expressed genes (DEGs) were identified using the "limma" package in R, with thresholds set at $|\log\text{FoldChange}| > 2$ and $P\text{-value} < 0.05$.

2.19 Cell culture and treatment

The RAW264.7 macrophage cell line (CL-0190) was obtained from Pricella (Wuhan, China) and cultured in Dulbecco's modified eagle medium (DMEM, A1443001, Gibco, Thermo Fisher Scientific, China) supplemented with 10% fetal bovine serum (FBS, 12483020, Gibco, Thermo Fisher Scientific, China). RAW264.7 macrophages were stimulated with LPS (200 ng/mL) for 12 h to induce M1 subtype differentiation, followed by pEVs treatment to further promote macrophage polarization. In selected experiments, RAW264.7 cells were pretreated for 30 min with either an anti-Cd36 antibody (2 mg/L) or the tyrosine kinase inhibitor PP2 (10 μM) before M1 macrophage polarization induction *in vitro* [26]. The experimental groups included: Control, LPS, LPS + pEVs, LPS + pEVs + shNC, LPS + pEVs + shCd36, LPS + pEVs + IgG, LPS + pEVs + anti-CD36, LPS + pEVs + PBS, and LPS + pEVs + PP2.

2.20 Lentiviral transduction

Lentivirus-mediated knockdown of Cd36 or Fyn in RAW264.7 macrophages was achieved using the pGreenPuro (CMV) shRNA Lentivector (sh-; Cat. No. SI505A-1, System Biosciences, USA), with a non-targeting vector used to generate control cells (shNC).

Experimental groups included shNC, shCd36-1, shCd36-2, shFyn-1, and shFyn-2. Lentiviral particles were produced by transfecting 293T cells (CRL-3216, ATCC, USA) with the corresponding shRNA constructs using Lipofectamine 3000 reagent (L3000015, Invitrogen, New York, CA, USA). After 20 h, the culture medium was replaced with 12 mL of medium supplemented with 5% FBS. Approximately 48 h later, the viral supernatant was harvested and filtered using a 0.45 μm cellulose acetate membrane filter (HAWG04700, MF-Millipore) and stored at −80 °C. For lentiviral infection of RAW264.7 cells, 5×10^5 cells were seeded in 6-well plates. When the confluency reached 70%–90%, the cells were infected with the packaged lentivirus (multiplicity of infection (MOI) = 10, viral titer ~ 5×10^6 TU/mL) in a medium containing 5 μg/mL polybrene (Merck, TR-1003, USA). After 4 h, an equal volume of fresh medium was added to reduce polybrene concentration. Culture medium was replaced 24 h after transduction. Transduction efficiency was evaluated at 48 h based on luciferase reporter expression, followed by selection with puromycin (60 μg/mL; E607054, Sangon Biotech, Shanghai, China). Knockdown efficiency was confirmed by western blot analysis, and successfully transduced cells were used for subsequent experiments. All conditions were analyzed in triplicate, and shRNA sequences are provided in Table S2 in the ESM.

2.21 CD36 expression and cell infection

A lentiviral expression plasmid encoding SFB-tagged CD36 was constructed and packaged into a lentivirus to infect RAW264.7 cells. Infected cells were lysed in a lysis buffer containing protease inhibitors (FNN0021, Thermo Fisher Scientific Inc., China). A total of 15 mL of cell lysate was incubated overnight at 4 °C with 300 μL of streptavidin-agarose beads (Strep-Beads). After three centrifugation steps, the supernatant was discarded. The pellet was then eluted with 1 mg/mL biotin (29129, Thermo Fisher Scientific Inc., China) and centrifuged to collect the supernatant. This supernatant was incubated with 50 μL of S protein agarose beads at 4 °C for 1 h, followed by centrifugation to collect the pellet. The interaction between FLAG-CD36 and HA-Fyn was analyzed via Western blot. Antibody information is provided in Table S1 in the ESM.

2.22 Reverse transcription-quantitative polymerase chain reaction (RT-qPCR)

Total RNA was extracted using Trizol reagent (15596026, Invitrogen, USA). RNA concentration and purity were assessed with a NanoDrop 2000 spectrophotometer (Thermo Fisher, USA) to confirm suitability for downstream applications. Reverse transcription was performed using the PrimeScript RT Reagent Kit (RR047A, Takara, Japan) under standardized conditions to generate complementary DNA. Quantitative PCR was carried out with the Fast SYBR Green PCR Kit (11736059, Thermo Fisher Scientific, China), with three technical replicates analyzed per sample. Glyceraldehyde-3-phosphate dehydrogenase (GAPDH) served as the internal reference gene, and relative expression levels were calculated using the $2^{-\Delta\Delta Ct}$ method. Standard curve analysis yielded coefficients of determination exceeding 0.99, indicating robust amplification efficiency. All experiments were independently repeated three times. Sample processing and data acquisition were performed in a blinded manner to minimize bias. Statistical analyses incorporated effect size estimation and were further evaluated using Bayesian approaches or multivariable regression to improve analytical rigor. Primer sequences used for RT-qPCR are provided in Table S3 in the ESM (synthesized by Takara).

2.23 Immunofluorescence

Cells for immunofluorescence analysis were seeded on glass coverslips in 12-well culture plates one day before staining. After cell attachment, culture medium was removed, and coverslips were washed three times with PBS for 5 min per wash. Cells were then fixed with 4% PFA, permeabilized with 0.1% Triton X-100, and blocked with 10% normal donkey serum. Lung tissue samples were fixed in 4% PFA, followed by dehydration, clearing, paraffin embedding, and sectioning. Tissue sections were deparaffinized, rehydrated, and blocked with 2% BSA. Primary antibodies were applied and incubated overnight at 4 °C (antibody details are listed in Table S1 in the ESM). After washing with PBS, sections were incubated with goat anti-mouse or goat anti-rabbit IgG secondary antibodies at room temperature for 1 h. Nuclei were counterstained with 4',6-diamidino-2-phenylindole (DAPI) (C1002, Beyotime, China) for 5 min, followed by three PBS washes to remove excess stain. Coverslips were mounted onto glass slides using antifade mounting medium. Fluorescence images were acquired with a fluorescence microscope (FV-1000/ES, Olympus, Japan). Quantitative analysis was performed by measuring fluorescence-positive areas under a 40× objective lens across six randomly selected fields per group, and mean values were calculated.

2.24 Western blot

Protein samples isolated from tissues and whole-cell lysates were quantified using the Pierce BCA Protein Assay Kit (23227, Thermo Fisher, USA). Tissue and cellular proteins were extracted using radioimmunoprecipitation assay (RIPA) lysis buffer. A total of 20 μg of protein per sample was loaded onto sodium dodecyl sulfate-polyacrylamide gel electrophoresis (SDS-PAGE) gels and subsequently transferred onto nitrocellulose membranes. After blocking with 5% non-fat milk for 1 h, the membranes were incubated with primary antibodies. On the following day, immunoreactive bands were visualized using an enhanced chemiluminescence reagent (WP20005, Thermo Fisher, USA) and imaged with the ChemiDoc XRS Plus luminescent imaging system (Bio-Rad). Band intensities were quantified using ImageJ software, with GAPDH used as the internal loading control (antibody details are listed in Table S1 in the ESM). All experiments were independently repeated three times.

2.25 Statistical analysis

Experimental data were obtained from at least three independent experiments and are presented as mean ± standard deviation (SD). Comparisons between two groups were performed using an independent samples *t*-test. A one-way analysis of variance (ANOVA) was applied for comparisons among three or more groups. Tukey's post hoc test was conducted for pairwise comparisons when ANOVA indicated significant differences. The Mann-Whitney U test or Kruskal-Wallis H test was employed for data not meeting normality or homogeneity of variance assumptions.

Statistical analyses were conducted using GraphPad Prism 9 (GraphPad Software, Inc.) and R version 4.2.1 within the RStudio environment. Perl version 5.30.0 was applied for data processing. A two-tailed *P*-value of less than 0.05 was considered statistically significant.

3 Results

3.1 Storage-related pEVs aggravated pulmonary inflammation and tissue injury in LPS-primed mice

To simulate the production and pathogenic effects of pEVs during clinical platelet storage, we successfully isolated pEVs from BALB/c mouse platelets using ultracentrifugation combined with filtration (Fig. S1(a) in the ESM). Storage-associated changes in platelet and pEV-related parameters were then systematically examined. Compared with freshly isolated platelets, prolonged storage resulted in a progressive decline in suspension pH (Fig. S1(b) in the ESM), accompanied by significant increases in LA and lactate dehydrogenase A (LDHA) levels (Figs. S1(c) and S1(d) in the ESM). In addition, the expression of the platelet activation marker CD62P gradually declined with increasing storage duration (Fig. S1(e) in the ESM). In contrast, thrombin-activated platelets exhibited a lower pH and higher levels of lactate, LDHA, and CD62P expression than fresh platelets (Figs. S1(b)–S1(e) in the ESM). TEM, NTA, and immunoblotting confirmed the vesicular morphology and enrichment of exosome-associated proteins in the isolated pEVs (Figs. S1(f)–S1(h) in the ESM). Quantitative analysis further demonstrated a time-dependent increase in pEV abundance in platelet suspensions across storage durations of D1, D3, and D5 (Fig. S1(i) in the ESM), indicating progressive accumulation of storage-associated pEVs.

Previous studies have reported that pEVs released during platelet storage may act as pathogenic factors in TRALI [27] and accelerate disease progression through endothelial injury [6]. To further investigate their pathogenic potential, we established a TRALI mouse model by combining LPS priming with pEVs administration (Fig. 1(a)). Clinical manifestations, physiological parameters, and tissue injury were systematically evaluated across experimental groups. Compared with the PBS control group, LPS alone induced typical TRALI-associated features, including labored respiration, irregular breathing, reduced mobility, and increased foamy secretions from the oral and nasal cavities. Co-administration of pEVs markedly exacerbated these symptoms, with the most severe responses observed in the D5 group (Fig. 1(b)). Oxygenation analysis revealed a significant reduction in arterial PO_2 levels in the LPS + pEVs group (Fig. 1(c)), along with a marked increase in total protein concentration in BALF (Fig. 1(d)), indicating aggravated pulmonary permeability impairment.

Survival analysis showed that 40% of mice in the LPS-treated group died within 80 h, whereas all mice in the LPS + pEVs (D5) group died within 50 h (Fig. 1(e)), indicating a marked increase in TRALI-associated mortality following pEV exposure in LPS-primed mice. Histopathological assessment revealed pronounced lung structural damage in the LPS group, characterized by alveolar wall disruption and infiltration of erythrocytes and inflammatory cells into alveolar spaces. Lung injury was further aggravated in the LPS + platelet group, and the LPS + pEVs group exhibited the most severe pathological damage, with the most severe damage observed in the D5 subgroup (Fig. 1(f)). Consistent with these findings, analysis of BALF showed elevated levels of the pro-inflammatory cytokines IL-6 and IL-12, and reduced expression of the anti-inflammatory cytokine IL-10 following LPS, LPS + platelet, and LPS + pEVs treatment. The strongest inflammatory response was detected in the LPS + pEVs (D5) group (Fig. 1(g)).

Collectively, these results establish a robust TRALI mouse model induced by combined LPS and pEV administration, and demonstrate that pEVs markedly aggravate pulmonary injury and inflammation in LPS-primed mice, providing a reliable *in vivo* framework for subsequent mechanistic studies.

3.2 scRNA-seq revealed macrophage dominance in the TRALI mouse model

To investigate the compositional changes and regulatory mechanisms of pulmonary immune cells in the TRALI mouse

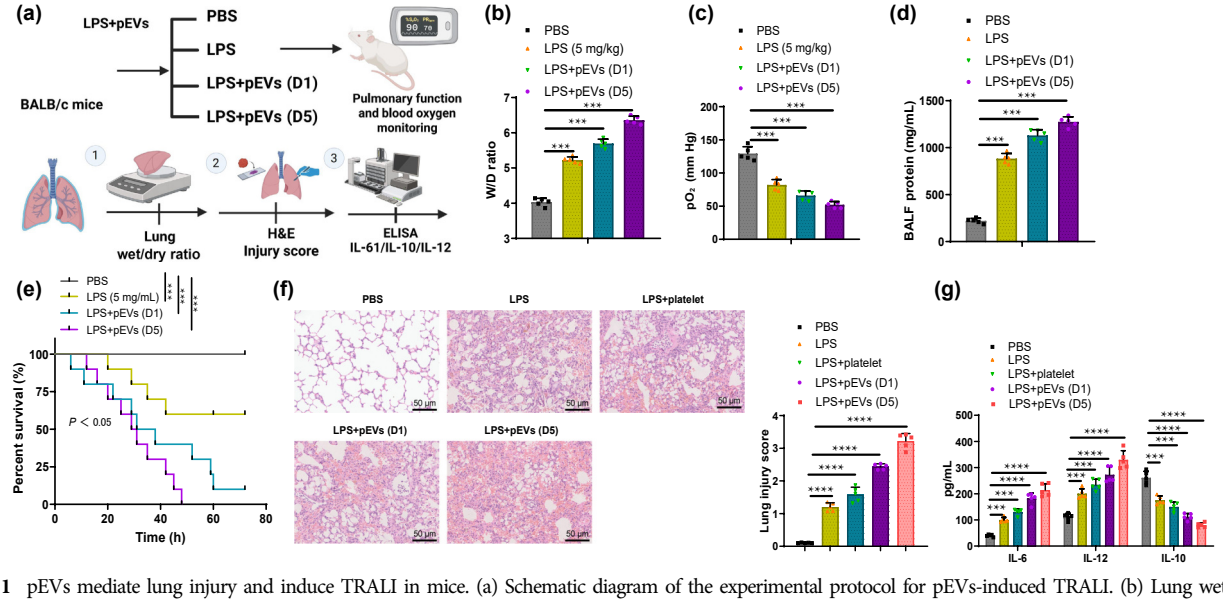

Figure 1 pEVs mediate lung injury and induce TRALI in mice. (a) Schematic diagram of the experimental protocol for pEVs-induced TRALI. (b) Lung wet-to-dry weight ratios under different treatment conditions (n = 5). (c) Measurement of arterial blood PO_2 (n = 5). (d) Protein concentration in BALF (n = 5). (e) Survival curves of mice under different treatments (n = 10). (f) H&E staining of lung tissues from different groups (scale bars = 50 μm) (n = 5). (g) ELISA measurement of inflammatory cytokines (IL-6, IL-12, and IL-10) in BALF (n = 5). Data in panels (b)–(d) and (g) are presented as mean ± SD. The survival curves in panel (e) were analyzed using the log-rank (Mantel–Cox) test. All intergroup comparisons were performed using one-way analysis of variance (ANOVA) followed by Tukey's post hoc multiple-comparison test. *P < 0.05, **P < 0.01, ***P < 0.001, ****P < 0.0001 versus the PBS group.

model induced by LPS combined with pEVs, we performed scRNA-seq on lung tissue from TRALI mice and PBS-injected controls (Fig. 2(a)). CD11b$^+$ mononuclear cells were enriched from lung tissue suspensions of two randomly selected TRALI mice using the 10× genomics chromium platform, followed by construction of single-cell cDNA libraries and high-throughput sequencing. Two mice from the PBS group served as controls (n = 2).

Raw scRNA-seq data were subjected to rigorous quality control and normalization (filtering criteria: nFeature_RNA > 200, nCount_RNA < 50,000, percent.mt < 10), and low-quality cells were excluded (Fig. S2(a) in the ESM). A total of 28,692 highly variable genes were identified, from which the top 2000 most variable genes were selected for downstream analyses (Fig. S2(b) in the ESM). PCA indicated that the first four components effectively separated major cell populations (Fig. S2(c) in the ESM). Based on the elbow plot, the top 17 PCs were retained for clustering (Fig. S2(d) in the ESM).

Using the Seurat package, we integrated multiple samples and corrected for batch effects. Dimensionality reduction was then performed using the t-SNE algorithm, identifying 16 distinct cell clusters. Cells were assigned to the TRALI or control group based on sample origin (Figs. S2(e) and S2(f) in the ESM). Cell type annotation was conducted using SingleR in combination with established marker genes. Major immune cell populations identified in lung tissue included macrophages (marker genes: *Tgfb1*, *Ccl2*, *Apoe*), monocytes (*Nr4a1*, *Ly6c2*, *Plac8*), and dendritic cells (DCs; *Crip1*, *Ccr7*, *Tmem123*) (Figs. 2(b) and 2(c)).

Further analysis of cell composition revealed that macrophages were the predominant immune cell type in the pulmonary microenvironment of TRALI and control groups, accounting for over 50% of the total immune cells (Figs. 2(d) and 2(e)), while monocytes and DCs represented smaller proportions.

Overall, single-cell transcriptomic profiling demonstrated macrophage predominance within the pulmonary immune landscape of the TRALI mouse model, suggesting their potential key role in the immune response induced by pEVs.

3.3 Pseudotime trajectory analysis revealed the dynamic expansion and dominant role of pro-inflammatory macrophages in TRALI

To further elucidate the heterogeneity of macrophage populations in the TRALI model and explore the potential roles of distinct subpopulations during disease progression, we conducted in-depth

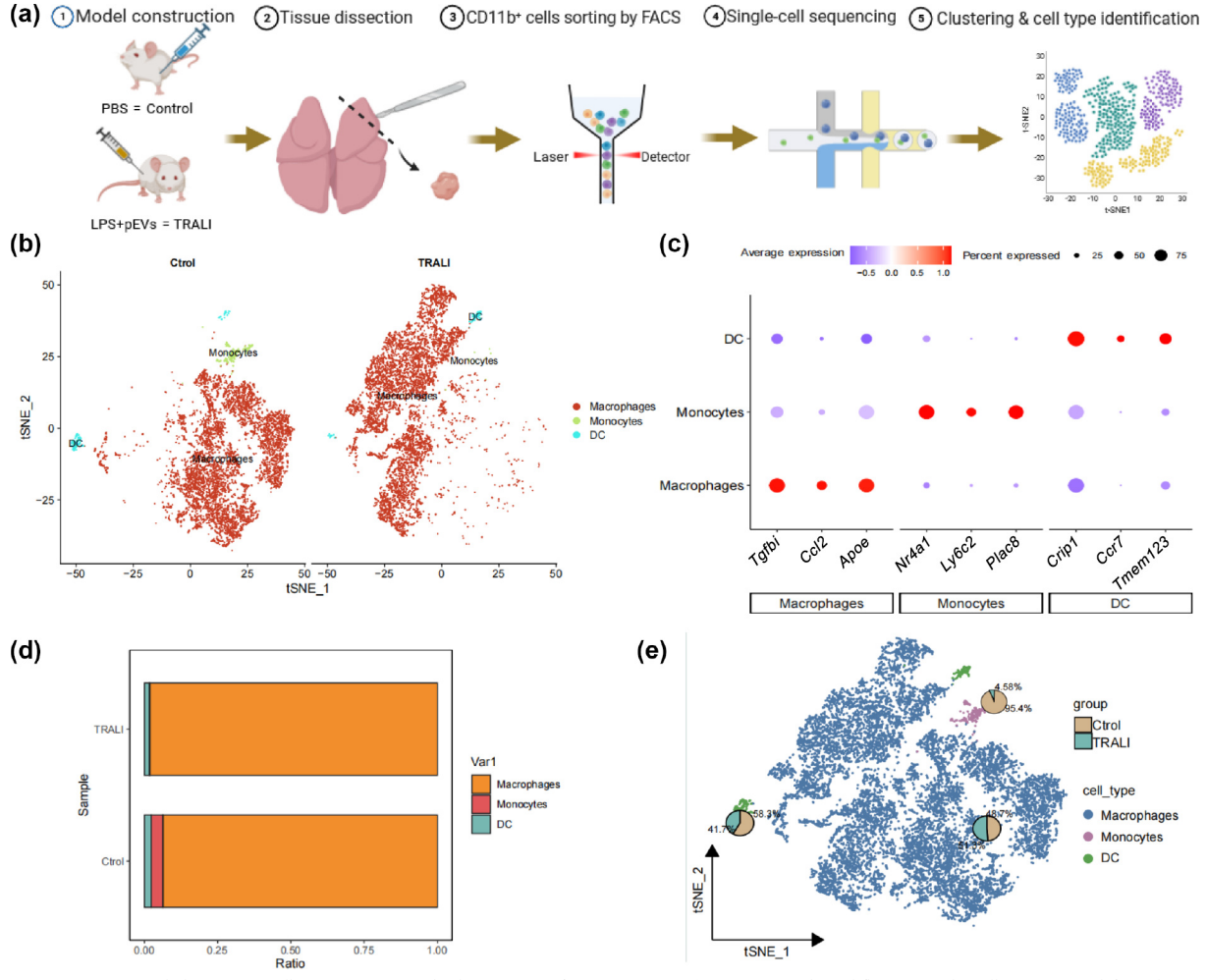

Figure 2 scRNA-seq revealed immune cell composition in the lung tissue of TRALI mice. (a) Experimental workflow: CD11b$^+$ cells were sorted from lung tissue of TRALI and PBS control mice and subjected to scRNA-seq using the 10× genomics chromium platform. (b) t-SNE clustering map showing cell subpopulation annotations after batch effect correction. (c) Distribution of major immune cell types (macrophages, monocytes, and DCs) in TRALI (n = 2) and control (n = 2) samples. (d) Bar plots show the relative proportions of the three main immune cell types across groups. (e) t-SNE plots further illustrate the spatial distribution of immune cell types between the two groups.

subclustering and pseudotime trajectory analyses of macrophages. Based on characteristic gene expression profiles, macrophages were classified into four subpopulations: *Fn1*$^+$ macrophages, *Folr2*$^+$ macrophages, *Hmox1*$^+$ macrophages, and *Stmn1*$^+$ macrophages (Figs. 3(a) and 3(b)).

Differentiation relationships and developmental dynamics among these subsets were subsequently explored using pseudotime analysis. Genes with an average expression level ≥ 0.1 were retained for further analysis (Fig. S3(a) in the ESM). A developmental trajectory was reconstructed using the Monocle algorithm, revealing four major branch points. Distinct distribution patterns were observed among macrophage subpopulations along the trajectory. *Stmn1*$^+$ macrophages were distributed across branches 2, 3, and 4, whereas Hmox1$^+$ macrophages were primarily enriched in branch 3. *Fn1*$^+$ macrophages were broadly distributed across branches 2, 3, and 4, with a predominant enrichment in branch 4. In contrast, *Folr2*$^+$ macrophages were almost exclusively localized at the beginning of the trajectory, suggesting representation of an early or precursor differentiation state (Figs. 3(c) and 3(d)). Further stratification of cell states identified nine developmental stages, illustrating progressive and dynamic shifts in macrophage composition along the pseudotime axis (Fig. 3(e) and Fig. S3(b) in the ESM).

Analysis of gene expression dynamics along pseudotime revealed relatively stable expression of the pan-macrophage marker Cd68. In contrast, expression of *Folr2*$^+$ macrophage markers, including *Mrc1* and *Csf1r*, gradually declined with pseudotime progression, whereas *Fn1*$^+$ macrophage markers such as *Ccr2* and *Il1b* exhibited a marked and continuous increase. The proliferation-associated gene *Mki67* showed selective and pronounced upregulation in the

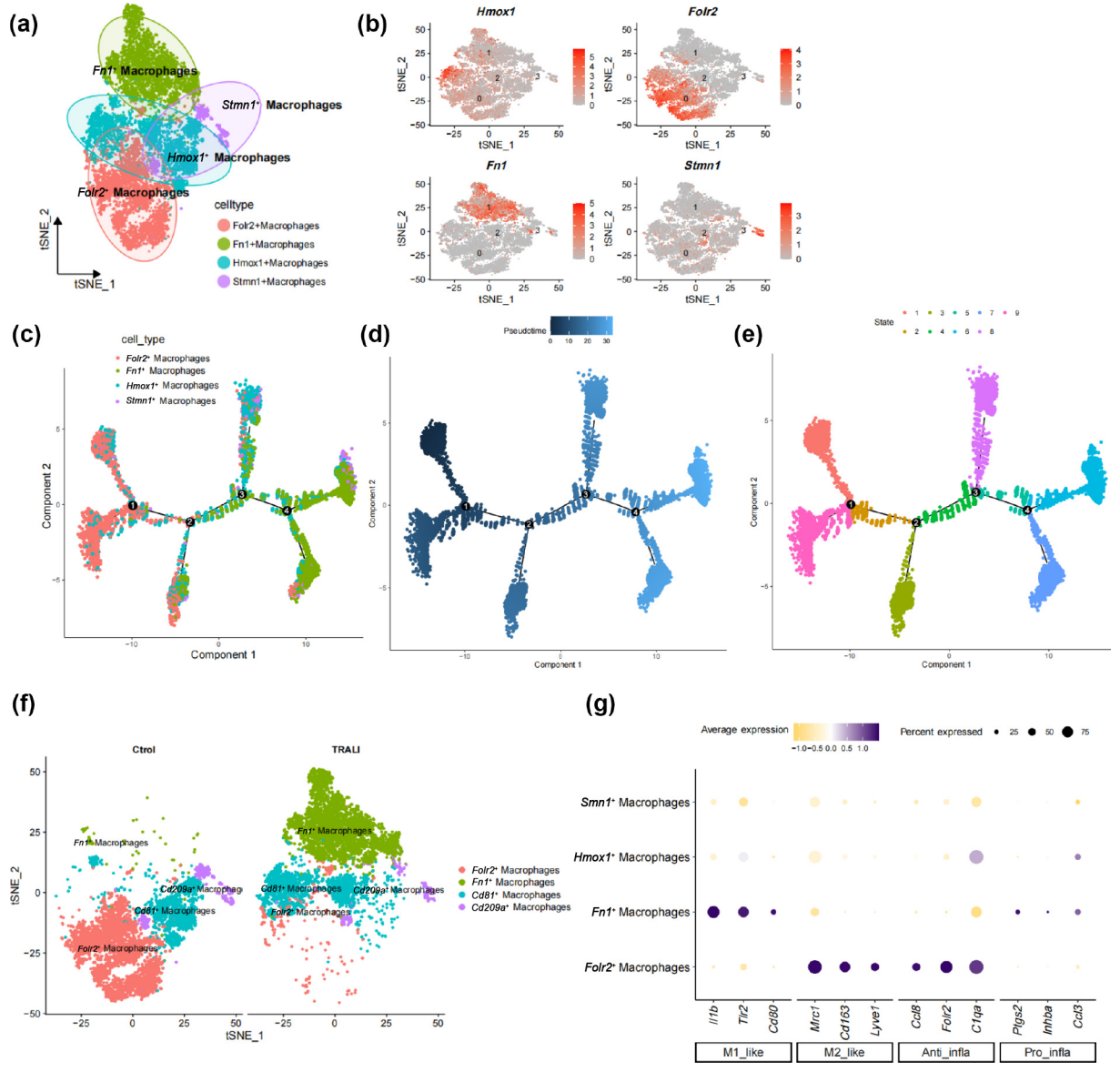

Figure 3 Subpopulation and pseudotime trajectory analysis of macrophages. (a) Visualization of four functional macrophage subpopulations (Fn1$^+$, Folr2$^+$, Hmox1$^+$, and Stmn1$^+$). (b) Heatmap showing the expression of signature marker genes in each subpopulation. (c) Distribution of the four subpopulations along the pseudotime developmental tree, colored by cluster identity. (d) Cell trajectory plot arranged by pseudotime, where each dot represents a single cell and the color gradient reflects pseudotime progression from the initial to terminal state. (e) Developmental trajectory divided into nine stages, illustrating cell distribution across different maturation states. (f) t-SNE plot showing the distribution of the four macrophage subpopulations between control and TRALI samples. (g) Bubble plot displaying the expression of M1/M2 phenotypic markers and pro-/anti-inflammatory genes across the macrophage subpopulations.

Stmn1$^+$ macrophage subset (Fig. S3(c) in the ESM). Across the four major branches of the trajectory, we further identified gene modules with distinct expression patterns and similar dynamic trends through clustering analysis (Fig. S3(d) in the ESM).

Analysis of macrophage subpopulation distribution across different experimental groups showed that Folr2$^+$ macrophages were predominantly present in the control group, whereas Fn1$^+$ macrophages were almost exclusively associated with the TRALI model. In contrast, Hmox1$^+$ and Stmn1$^+$ macrophages were detected in both groups without an obvious distributional bias (Fig. 3(f)). Functional phenotype analysis further confirmed that Folr2$^+$ macrophages exhibited anti-inflammatory M2-like features, while Fn1$^+$ macrophages displayed classical pro-inflammatory M1-like characteristics (Fig. 3(g)).

Collectively, single-cell transcriptomic pseudotime trajectory analysis demonstrated a pronounced expansion and dominance of Fn1$^+$ pro-inflammatory M1 macrophages in the pEVs-induced TRALI model, supporting a central regulatory role for this macrophage subset in driving TRALI-associated immunopathological progression.

3.4 pEVs induced M1 macrophage polarization and enhanced inflammatory phenotypes *in vitro* and *in vivo*

To determine the role of pEVs in macrophage polarization, we first established an *in vitro* LPS-induced M1 polarization model. RAW264.7 macrophages were exposed to pEVs (D5) in combination with LPS for 48 h, followed by assessment of polarization status (Fig. 4(a)). Flow cytometric analysis demonstrated a significant increase in expression of the M1-associated surface marker CD86 and a markedly reduction in the LPS + pEVs group (Fig. 4(b)), indicating that pEVs significantly enhanced LPS-induced M1 polarization.

Further analysis using RT-qPCR showed that expression levels of M1-associated inflammatory factors, including iNOS and TNF-α, were significantly upregulated in the LPS + pEVs group, whereas M2-associated factors IL-10 and Arg-1 were downregulated (Fig. 4(c)). ELISA analysis further demonstrated increased secretion of IL-6 and IL-12 together with reduced IL-10 production in the LPS + pEVs group, further supporting the role of pEVs in promoting M1 polarization (Fig. 4(d)).

To determine whether similar effects occurred *in vivo*, we established an LPS + pEVs-induced TRALI mouse model (Fig. 4(e)). IVIS fluorescence imaging revealed that DiI-labeled pEVs predominantly accumulated in the lungs, with lower signal intensity detected in the liver and spleen, indicating preferential pulmonary distribution of pEVs (Fig. 4(f)). Flow cytometry analysis further confirmed that the proportion of M1 macrophages (CD86$^+$) was significantly increased, whereas M2 macrophages (CD206$^+$) were significantly reduced in the lung tissue of TRALI mice (Fig. 4(g)).

Consistent with these observations, RT-qPCR analysis revealed elevated expression of the M1-associated markers TNF-α and iNOS, accompanied by downregulation of the M2-associated markers IL-10 and Arg-1 in lung tissue (Fig. 4(h)). Immunofluorescence staining confirmed these molecular changes, showing increased iNOS expression and reduced Arg-1 levels in the TRALI model (Fig. 4(i)).

Collectively, these findings demonstrate that pEVs potentiate LPS-induced M1 macrophage polarization *in vitro* and drive a shift toward a pro-inflammatory M1 phenotype in pulmonary macrophages *in vivo*, supporting a critical role for pEVs in amplifying inflammation and promoting TRALI pathogenesis.

3.5 Key mechanism by which Cd36 mediates pEVs-induced M1 macrophage polarization

To identify key genes involved in regulating macrophage function during the progression of TRALI, we first performed differential gene expression analysis of lung macrophages from normal control mice and those with pEVs + LPS-induced TRALI based on scRNA-seq data. A total of 1978 DEGs were identified (Fig. S4(b), and Table S4 in the ESM). In addition, we collected BALF from both control and TRALI groups, isolated macrophages via antibody labeling and cell sorting, and performed bulk transcriptome sequencing (Fig. S4(a) in the ESM), yielding 296 DEGs (Fig. S4(c), and Table S5 in the ESM). Intersection analysis revealed five overlapping candidate genes: *Ccl8*, *Cd36*, *Tnrc6b*, *Pbx3*, and *Rasa1* (Fig. S4(d) in the ESM). Among these, *Cd36*, *Tnrc6b*, and *Rasa1* were significantly upregulated in TRALI samples, while *Ccl8* and *Pbx3* were downregulated (Fig. S4(e) in the ESM). Gene Ontology (GO) enrichment analysis indicated predominant involvement in biological processes related to cell–matrix adhesion (Fig. S4(f), and Table S6 in the ESM). Previous studies have demonstrated that Cd36, a macrophage membrane receptor, regulates mitochondrial metabolism and amplifies inflammatory responses, supporting a potential role in M1 polarization [28].

Single-cell transcriptomic analysis further demonstrated marked enrichment of Cd36 expression in Fn1$^+$ macrophages, an M1-like subpopulation, within TRALI samples, whereas minimal expression was detected in control lungs (Fig. 5(a)), suggesting that Cd36 may serve as a key target in pEVs-mediated macrophage polarization. To validate this possibility, Cd36 expression was examined in lung tissue from mice subjected to the LPS + pEVs two-hit TRALI model (Fig. 5(b)). RT-qPCR results showed that both LPS and pEVs alone upregulated Cd36 mRNA expression in lung tissue, with combined treatment producing a more pronounced upregulation (Fig. 5(c)). Immunofluorescence analysis further confirmed that Cd36 was primarily localized in lung macrophages and was markedly upregulated in the TRALI model group (Fig. 5(d)).

In vitro experiments demonstrated that pEVs treatment markedly increased Cd36 expression in RAW264.7 cells (Fig. 5(e)). To further elucidate the role of Cd36 in pEVs-induced M1 polarization, we inhibited Cd36 expression using shRNA-mediated gene silencing and antibody-based functional blockade (Fig. 5(f)). Western blot analysis confirmed efficient Cd36 knockdown (Fig. S5(a) in the ESM). Functional assays demonstrated that Cd36 silencing markedly suppressed the M1 polarization phenotype induced by LPS + pEVs, as evidenced by significantly reduced mRNA levels of TNF-α and iNOS (Fig. 5(g)), as well as decreased protein levels of IL-6 and IL-12 (Fig. 5(h)). Additionally, flow cytometry revealed a significant reduction in the proportion of CD86$^+$ cells (Fig. 5(i)). Similarly, treatment with a CD36-blocking antibody inhibited Cd36 expression in RAW264.7 cells (Fig. S5(b) in the ESM). Under antibody-mediated blockade, pEVs-induced upregulation of iNOS, TNF-α, IL-6, and IL-12 was significantly suppressed (Figs. 5(j) and 5(k)), accompanied by a marked decrease in the proportion of CD86$^+$ cells (Fig. 5(l)).

In vivo and *in vitro* results consistently support that Cd36 plays a critical regulatory role in pEVs-mediated M1 macrophage polarization. Cd36 may serve as a key molecular link between pEV

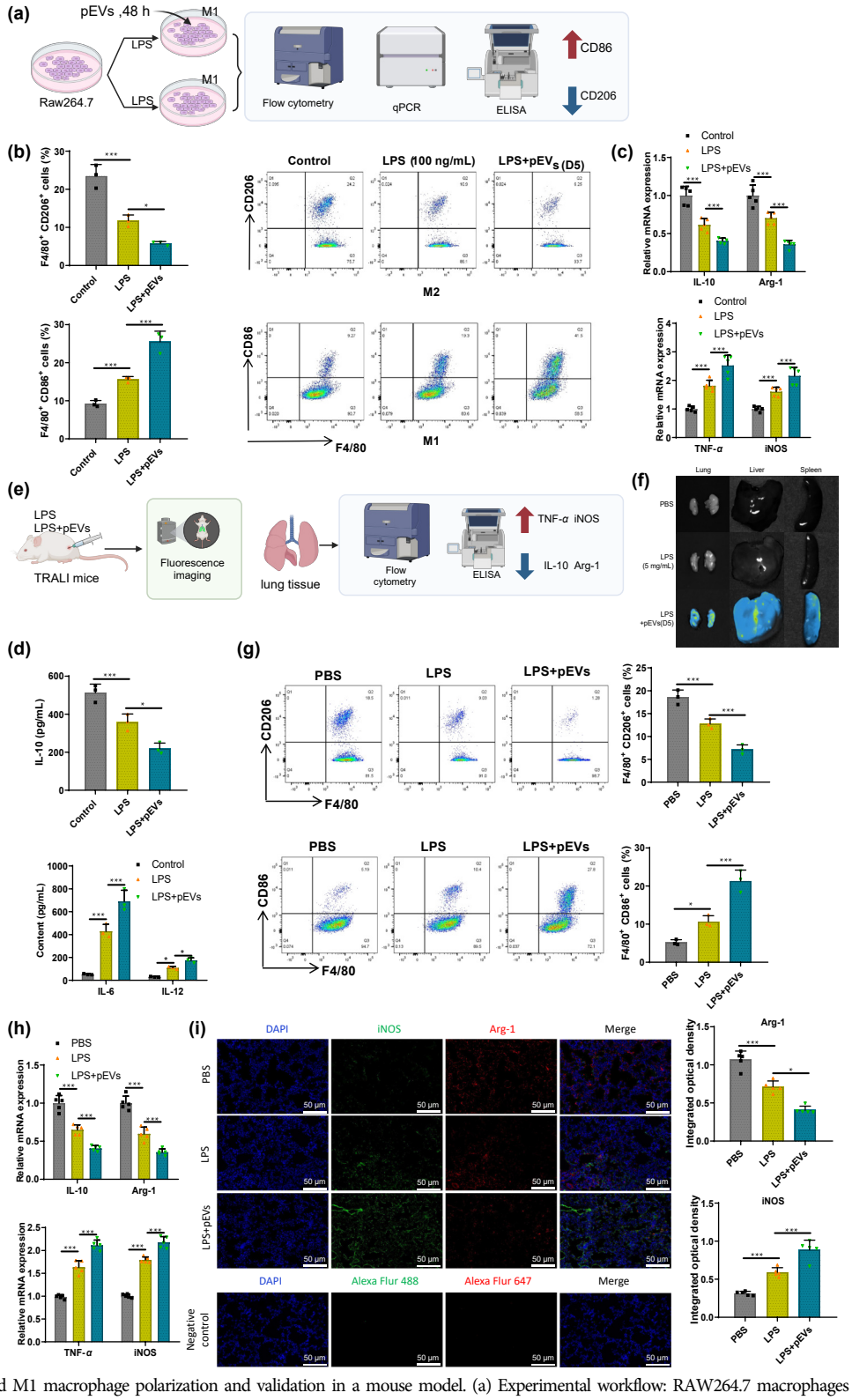

Figure 4 pEVs-induced M1 macrophage polarization and validation in a mouse model. (a) Experimental workflow: RAW264.7 macrophages were treated with LPS (200 ng/mL) and pEVs (D5) for 48 h, followed by flow cytometry, RT-qPCR, and ELISA. (b) Flow cytometry analysis of M1 ($CD86^+$) and M2 ($CD206^+$) macrophage proportions ($n = 3$). (c) RT-qPCR analysis of mRNA expression for M1 markers (iNOS, TNF-α) and M2 markers (IL-10, Arg-1) ($n = 5$). (d) ELISA for cytokines IL-6, IL-12, and IL-10 ($n = 3$). (e) *In vivo* experimental workflow: TRALI mouse model established via tail vein injection of LPS and/or pEVs, followed by lung tissue collection for analysis. (f) Fluorescence imaging showing that DiI-labeled pEVs predominantly accumulated in lung tissue, with minor distribution in the liver and spleen. (g) Flow cytometry analysis of M1 ($CD86^+$) and M2 ($CD206^+$) macrophages in mouse lung tissue ($n = 3$). (h) RT-qPCR analysis of M1-related genes (TNF-α, iNOS) and M2-related genes (IL-10, Arg-1) in lung tissue ($n = 5$). (i) Immunofluorescence staining of iNOS and Arg-1 protein expression in lung tissue (scale bars = 50 μm) ($n = 5$). Data in panels (b)–(i) are presented as mean ± SD. All intergroup comparisons were performed using one-way analysis of variance (ANOVA) followed by Tukey's post hoc multiple-comparison test. $^*P < 0.05$, $^{**}P < 0.01$, $^{***}P < 0.001$ versus the Control or PBS group. *In vitro* experiments were repeated at least three times.

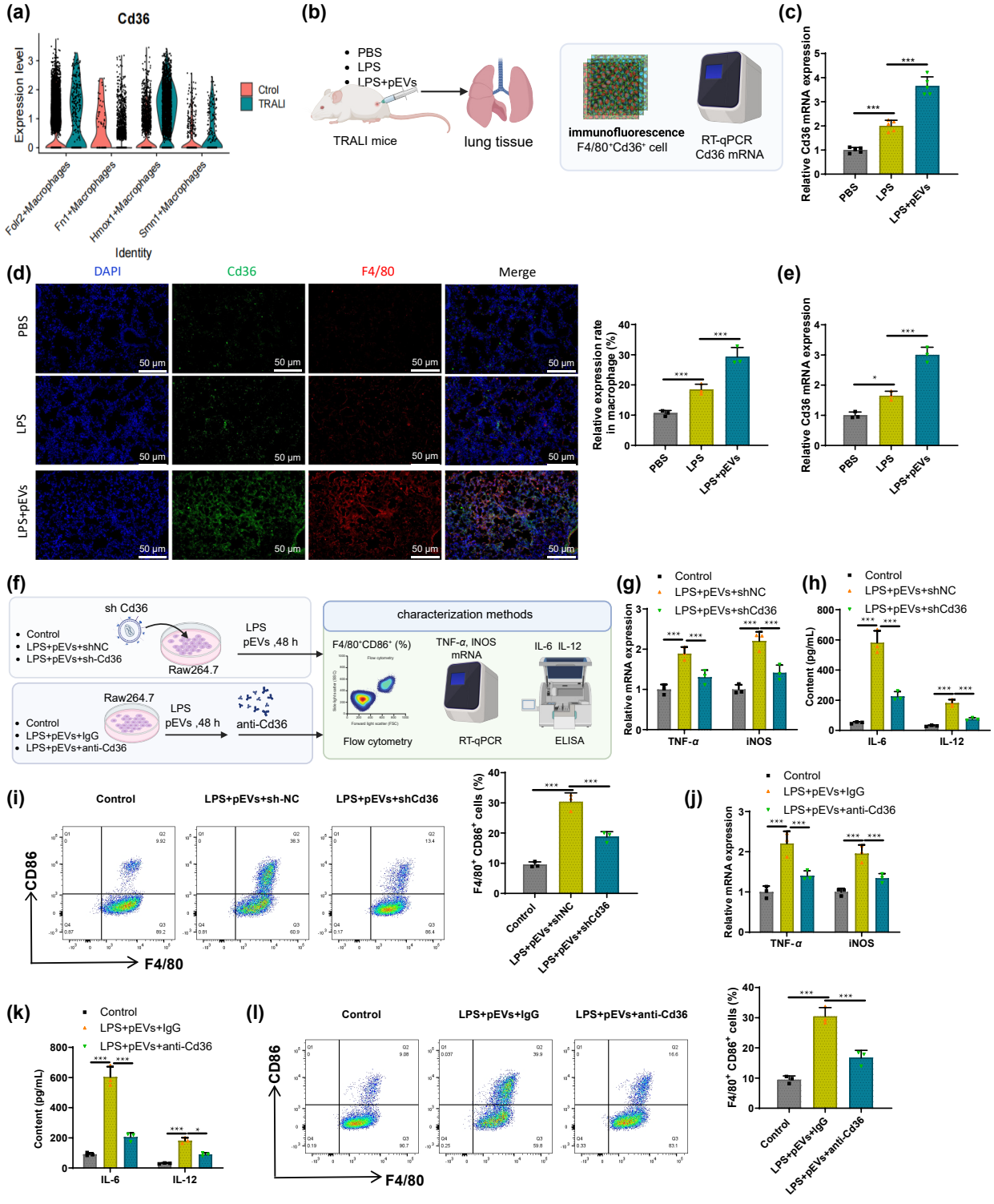

Figure 5 Investigation of Cd36 as a key regulator of pEVs-induced M1 macrophage polarization. (a) Violin plot showing the expression of Cd36 in the Fn1$^+$ macrophage subpopulation within lung tissue of TRALI mice based on scRNA-seq. (b) Schematic illustration of the *in vivo* experimental workflow for the TRALI mouse model. (c) RT-qPCR analysis of Cd36 mRNA expression in lung tissue from different treatment groups (n = 5). (d) Immunofluorescence staining and quantitative analysis of Cd36 protein in lung macrophages (scale bars = 50 μm) (n = 3). (e) RT-qPCR analysis of Cd36 mRNA expression in RAW264.7 cells under different treatments (n = 3). (f) Experimental workflow of gene knockdown and antibody blockade interventions. (g) RT-qPCR analysis of M1-associated genes (TNF-α, iNOS) in RAW264.7 cells after Cd36 silencing (n = 3). (h) ELISA measurement of IL-6 and IL-12 protein levels in RAW264.7 cells following Cd36 knockdown (n = 3). (i) Flow cytometry analysis of the proportion of CD86$^+$ cells in RAW264.7 cells after Cd36 silencing (n = 3). (j) RT-qPCR analysis of M1-related genes (TNF-α, iNOS) following CD36 antibody blockade in RAW264.7 cells (n = 3). (k) ELISA measurement of IL-6 and IL-12 protein levels following CD36 antibody blockade in RAW264.7 cells (n = 3). (l) Flow cytometry analysis of the proportion of CD86$^+$ cells following CD36 antibody blockade in RAW264.7 cells (n = 3). Data in panels (c)–(e) and (g)–(l) are presented as mean ± SD. All intergroup comparisons were performed using one-way analysis of variance (ANOVA) followed by Tukey's post hoc multiple-comparison test. *P < 0.05, **P < 0.01, ***P < 0.001. All *in vitro* experiments were repeated three times.

signaling and pro-inflammatory M1 responses, providing a novel mechanistic perspective on the pathogenesis of TRALI.

3.6 CD36 mediates pEVs-induced lung injury by regulating Fyn activity

To further investigate the downstream signaling mechanism of CD36, we first analyzed its protein structure using the SMART tool and identified multiple potential tyrosine kinase recognition sites in the cytoplasmic domain of CD36. Protein–protein interaction predictions based on the Search Tool for the Retrieval of Interacting Genes/proteins (STRING) database suggested a potential direct interaction between CD36 and Fyn, a member of the Src family kinases (Fig. 6(a)). The functional domains and critical phosphorylation sites of Fyn are illustrated in Fig. 6(b). Fyn has been implicated in diverse forms of tissue injury and is closely linked to oxidative stress, inflammasome activation, and endoplasmic reticulum stress, contributing to pathological processes in liver, kidney, and lung injury (Fig. 6(c)). Pharmacological inhibition of Fyn activity has been reported to mitigate LPS-induced organ damage. Based on these observations and bioinformatic predictions, CD36 was hypothesized to participate in pEVs-induced pulmonary immune injury through regulation of Fyn activity.

Confocal immunofluorescence analysis demonstrated that CD36 and Fyn were co-localized at the cell membrane and in the cytoplasm of RAW264.7 cells (Fig. 6(d)). Furthermore, co-immunoprecipitation (Co-IP) assays confirmed that CD36 and Fyn formed a protein complex under combined LPS and pEVs treatment, indicating a direct physical interaction between the two proteins (Fig. 6(e)).

To assess whether CD36 influences Fyn activation, phosphorylation status at key regulatory tyrosine residues was examined. Prior studies have established that phosphorylation at Tyr420 and dephosphorylation at Tyr531 correlate with enhanced Fyn kinase activity [29, 30]. Following LPS + pEVs stimulation, RAW264.7 cells exhibited increased phosphorylation at Fyn Tyr420, reduced phosphorylation at Tyr531, and elevated total Fyn protein levels. In contrast, Cd36 knockdown resulted in decreased Tyr420 phosphorylation, increased Tyr531 phosphorylation, and reduced total Fyn expression (Fig. 6(f)). These findings indicate that CD36 promotes Fyn kinase activation by modulating its phosphorylation dynamics (Fig. 6(g)).

To investigate the role of Fyn in M1 polarization, we inhibited its expression and activity using shRNA knockdown and the small-molecule inhibitor PP2 (Fig. 6(h)). Western blot confirmed efficient Fyn silencing (Fig. S5(c) in the ESM). Functional assays demonstrated that Fyn knockdown markedly attenuated pEVs-induced M1 polarization, as indicated by reduced mRNA expression of TNF-α and iNOS, decreased protein levels of IL-6 and IL-12 (Figs. 6(i) and 6(j)), and a lower proportion of $CD86^+$ cells (Fig. 6(k)). Similarly, PP2 treatment effectively reduced M1 marker expression (Figs. 6(l) and 6(m)), and markedly inhibited the M1 phenotype (Fig. 6(n)). Western blot analysis further confirmed that PP2 effectively suppressed Fyn Tyr420 phosphorylation (Fig. S5(d) in the ESM).

Collectively, these findings demonstrate that CD36 drives pEVs-induced M1 macrophage polarization through regulation of Fyn kinase activity, characterized by enhanced phosphorylation at Tyr420 and reduced phosphorylation at Tyr531. The CD36–Fyn signaling axis represents a critical immunomodulatory pathway in TRALI-associated lung injury and provides mechanistic insight that may inform the development of targeted therapeutic strategies for TRALI.

3.7 Targeting Cd36–Fyn exhibited therapeutic effects in the TRALI mouse model

Given the established role of the Cd36–Fyn signaling axis in pEVs-induced M1 macrophage polarization and TRALI progression, the therapeutic potential of targeting this pathway was further evaluated *in vivo* (Fig. 7(a)). We first constructed two-hit TRALI mouse models using Cd36 and Fyn knockout mice stimulated with pEVs (Figs. S6(a) and S6(b) in the ESM). Compared with wild-type TRALI mice, deficiency of Cd36 or Fyn significantly improved lung injury phenotypes, as evidenced by reduced lung wet-to-dry weight ratios, decreased protein leakage into BALF, increased arterial PO_2, and prolonged survival (Figs. 7(b)–7(f)).

Further analysis of the pulmonary immune microenvironment revealed that Cd36 or Fyn knockout significantly suppressed the expression of M1 macrophage markers (CD86, iNOS) and reduced the release of pro-inflammatory cytokines (TNF-α, IL-6). Interestingly, levels of the anti-inflammatory cytokine IL-10 were also moderately decreased (Figs. 7(g)–7(i)), indicating that disruption of the Cd36–Fyn signaling axis effectively attenuated M1 macrophage overactivation and associated inflammatory responses.

To explore potential therapeutic strategies, we administered a CD36-neutralizing antibody (intravenously) and the Fyn kinase inhibitor PP2 (intraperitoneally) as separate interventions (Fig. 8(a)). Both treatments independently alleviated TRALI-associated pathological injury, as demonstrated by reduced pulmonary edema, decreased protein leakage into alveolar spaces, improved oxygenation, and enhanced survival (Figs. 8(b)–8(f), and Figs. S6(c) and S6(d) in the ESM). Moreover, both interventions significantly suppressed M1 macrophage polarization markers (CD86, iNOS) and inflammatory cytokines (TNF-α, IL-6) (Figs. 8(g)–8(j)). Notably, combined treatment with CD36 antibody and PP2 exhibited a synergistic effect, further improving lung tissue repair and modulating the immune microenvironment more effectively.

Collectively, these results demonstrate that therapeutic targeting of the Cd36–Fyn signaling pathway effectively mitigates TRALI-associated lung injury by restraining M1 macrophage polarization, highlighting a promising strategy for future clinical intervention.

4 Discussion

TRALI represents one of the most severe adverse events associated with blood transfusion. Due to its complex and incompletely defined immunopathological mechanisms, effective and specific therapeutic options remain unavailable in clinical practice, resulting in persistently poor patient outcomes [3, 31, 32]. In recent years, preliminary studies have explored the pathogenesis of TRALI from multiple perspectives, including inflammatory responses, cytokine storms, and alveolar epithelial injury [33–35]. In contrast to existing studies, our work focused on the pivotal role of pEVs released during platelet storage in the development of TRALI. By establishing an LPS + pEVs-induced TRALI mouse model and integrating single-cell transcriptomic analysis, we comprehensively investigated immune cell composition in lung tissue and its underlying molecular mechanisms. The findings demonstrate that pEVs drive pro-inflammatory M1 macrophage polarization

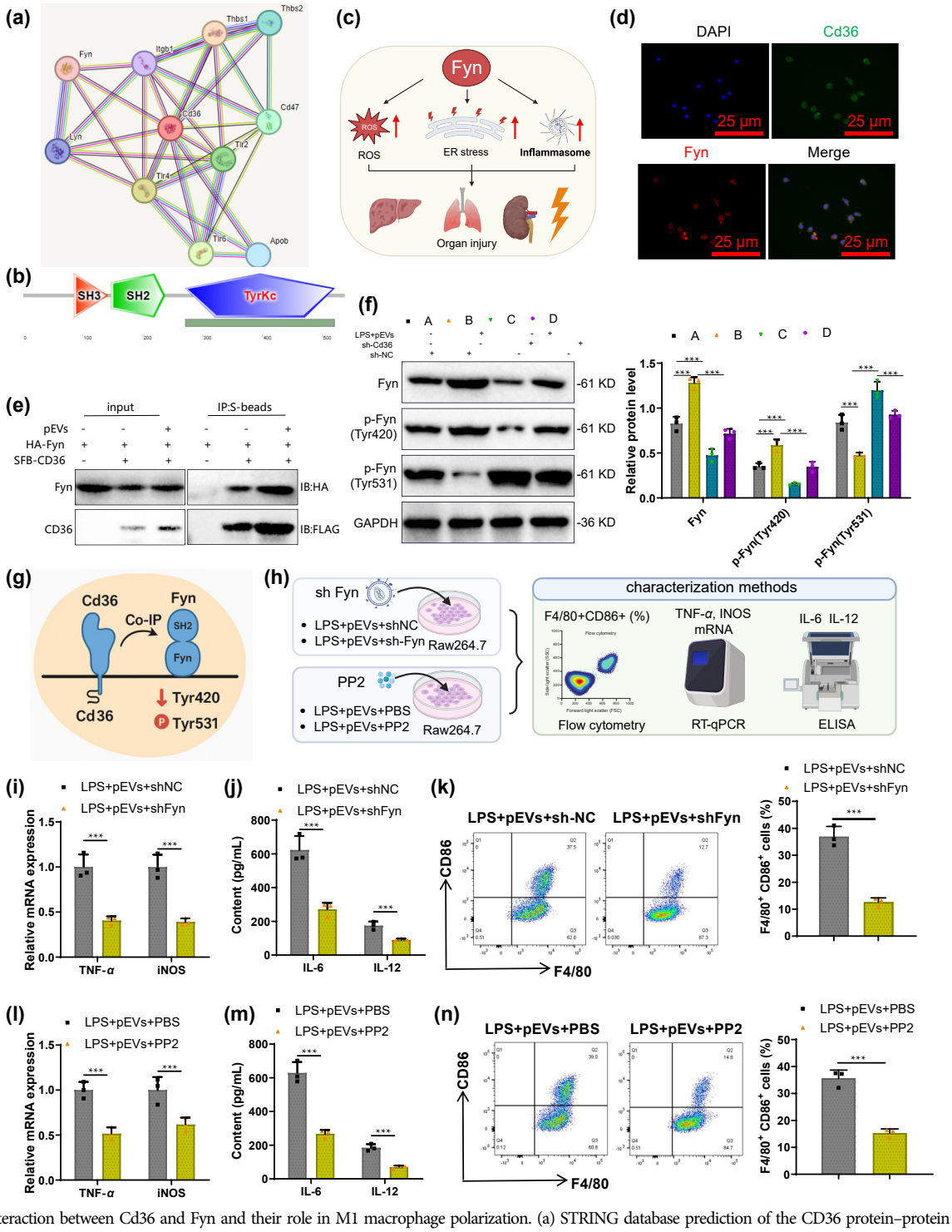

Figure 6 Interaction between Cd36 and Fyn and their role in M1 macrophage polarization. (a) STRING database prediction of the CD36 protein–protein interaction network; line thickness represents interaction confidence, and line color indicates the source of supporting evidence. (b) Schematic of the Fyn protein domain structure, highlighting key regions related to tyrosine kinase activity and phosphorylation sites (Tyr420 and Tyr531). (c) Diagram illustrating the role of Fyn kinase in inflammatory diseases such as liver and kidney injury. (d) Confocal immunofluorescence showing colocalization of CD36 (green) and Fyn (red) in RAW264.7 cells (nuclei stained with DAPI, scale bars = 25 μm). (e) Co-IP confirming the interaction between CD36 and Fyn upon LPS + pEVs stimulation (input: total protein; IP: immunoprecipitated complex). (f) Western blot analysis of total Fyn protein and its phosphorylation at Tyr420 and Tyr531 (n = 3). (g) Schematic model illustrating how CD36 regulates Fyn kinase activity by promoting Tyr420 phosphorylation and suppressing Tyr531 phosphorylation. (h) Workflow for genetic silencing and pharmacological inhibition of Fyn in functional assays. (i) RT-qPCR analysis of M1 marker genes (TNF-α, iNOS) following Fyn knockdown (n = 3). (j) ELISA quantification of IL-6, and IL-12 levels in the supernatant after Fyn knockdown (n = 3). (k) Flow cytometry analysis of the proportion of $CD86^+$ M1 macrophages after Fyn knockdown (n = 3). (l) RT-qPCR analysis of M1/M2-related gene expression following treatment with the Fyn inhibitor PP2 (n = 3). (m) ELISA analysis of IL-6, IL-12, and IL-10 levels in supernatants following PP2 treatment (n = 3). (n) Flow cytometry evaluation of CD86 expression following PP2 treatment (n = 3). Data in panel (f) are presented as mean ± SD. All intergroup comparisons for panel (f) were performed using one-way analysis of variance (ANOVA) followed by Tukey's post hoc multiple-comparison test. $^*P < 0.05$, $^{**}P < 0.01$, $^{***}P < 0.001$. All *in vitro* experiments were independently repeated three times.

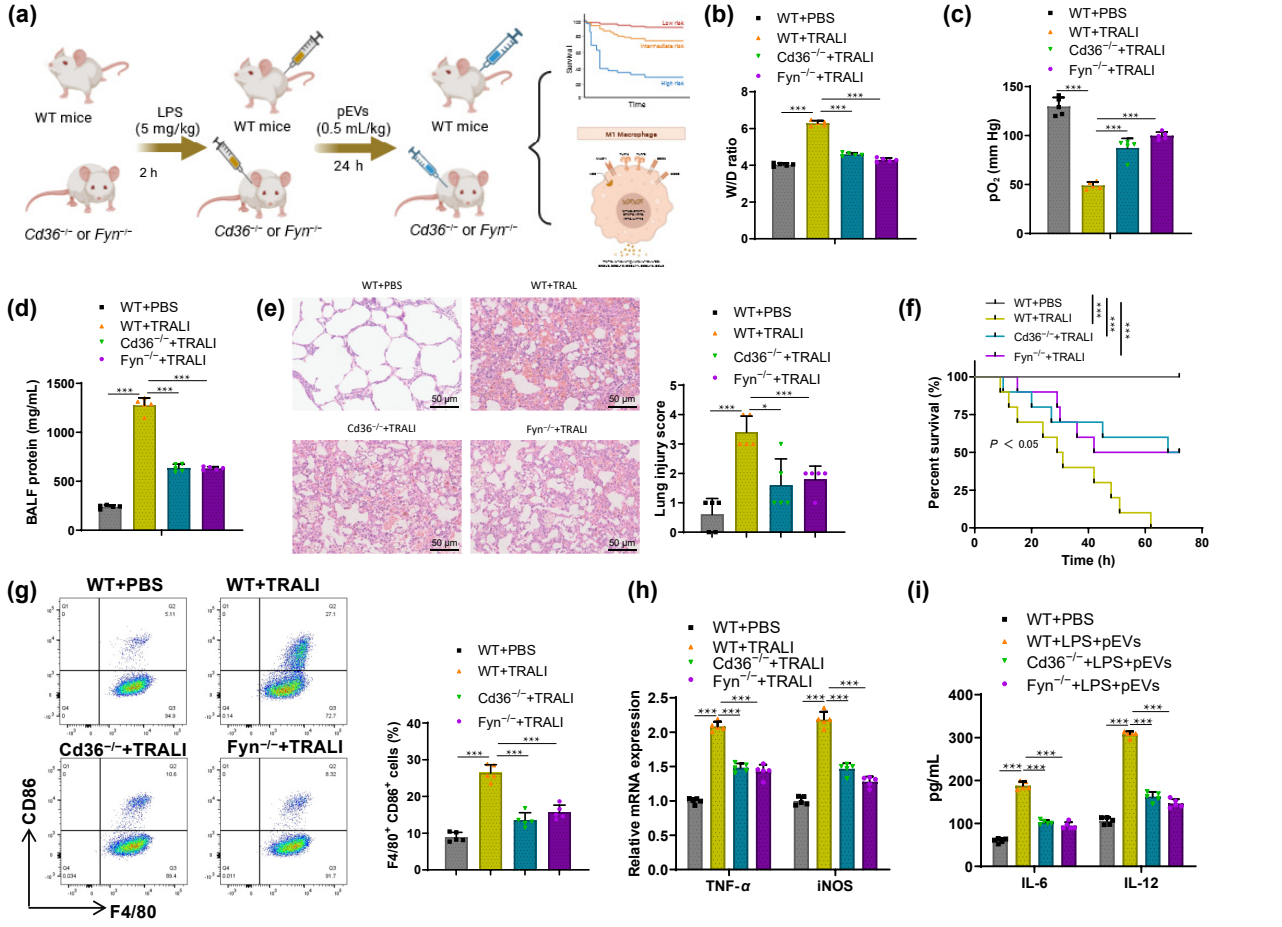

Figure 7 Effects of Cd36-Fyn deficiency in a pEVs-induced two-hit TRALI mouse model. (a) Workflow for evaluating the effect of targeting the Cd36-Fyn axis and modulating macrophage M1 polarization on the prevention and treatment of TRALI. (b) Lung wet-to-dry weight ratios in mice under different treatments (n = 5). (c) Arterial blood PO_2 measurement (n = 5). (d) Protein concentration in BALF (n = 5). (e) H&E staining of lung tissue under different treatments (scale bars = 50 μm) (n = 5). (f) Survival curves of mice under various treatment conditions (n = 10). (g) Flow cytometry detection of CD86 expression as an M1 macrophage marker in lung tissue (n = 5). (h) RT-qPCR analysis of M1-related gene expression in lung tissue (n = 5). (i) ELISA measurement of inflammatory cytokines (IL-6, IL-12) in BALF (n = 5). Data in panels (b)–(e) are presented as mean ± SD. The survival curves in panel (f) were analyzed using the log-rank (Mantel–Cox) test. All intergroup comparisons were performed using one-way analysis of variance (ANOVA) followed by Tukey's post hoc multiple-comparison test. $^*P < 0.05$, $^{**}P < 0.01$, $^{***}P < 0.001$.

through activation of the CD36–Fyn signaling axis, thereby identifying a previously underappreciated immunoregulatory pathway that contributes to TRALI pathogenesis.

TRALI was first described in 1957 and was initially associated with high-titer leukocyte antibodies. In 1983, the condition was formally defined as a clinical syndrome mediated by antibodies against human leukocyte antigens [7]. Subsequent studies expanded the pathogenic framework of TRALI to include additional contributors, such as antibodies against human neutrophil antigens, soluble CD40 ligand, and lysophosphatidylcholine [8, 9]. Notably, retrospective cohort studies have shown that patients with pre-existing pulmonary fibrosis, cardiovascular disease, or hematologic malignancies exhibit a substantially increased risk of TRALI following transfusion [36, 37]. Among patients admitted to intensive care units, reported TRALI-associated mortality rates reach as high as 70%, likely due to underlying comorbidities and systemic inflammatory status [38]. Therefore, identifying high-risk populations and elucidating the mechanisms underlying TRALI are critical for improving patient prognosis.

The findings of this study were highly consistent with previous literature and further confirmed the critical contribution of pEVs to the pathogenesis of TRALI [14]. A pronounced expansion of pro-inflammatory M1 macrophages was observed in the LPS + pEVs–induced TRALI mouse model, accompanied by marked upregulation of the macrophage marker Cd36. Previous studies have shown that the CD36–Fyn signaling axis participates not only in TRALI but also in macrophage-driven inflammatory polarization in disorders such as NASH and atherosclerosis [39], supporting a broader role for this pathway in inflammatory regulation. Previous evidence has documented that pEVs carry oxidized phospholipids (such as oxLDL-related components) or phosphatidylserine on their surface, both of which are high-affinity ligands for CD36. CD36 is a class B scavenger receptor capable of recognizing oxidized lipids and phosphatidylserine, thereby triggering conformational changes in CD36 [40]. Consistent with these observations, our Co-IP assays demonstrated that CD36 directly interacted with Fyn following LPS + pEVs stimulation, leading to increased phosphorylation at Fyn's activation site Tyr420 and decreased phosphorylation at its inhibitory site Tyr531, thereby activating its tyrosine kinase function [29, 30]. Activated Fyn has been reported to amplify inflammatory signaling through downstream nuclear factor kappa-B (NF-κB) and mitogen-activated protein kinase (MAPK) pathways, leading to excessive cytokine production [41]. In contrast, platelets generated after

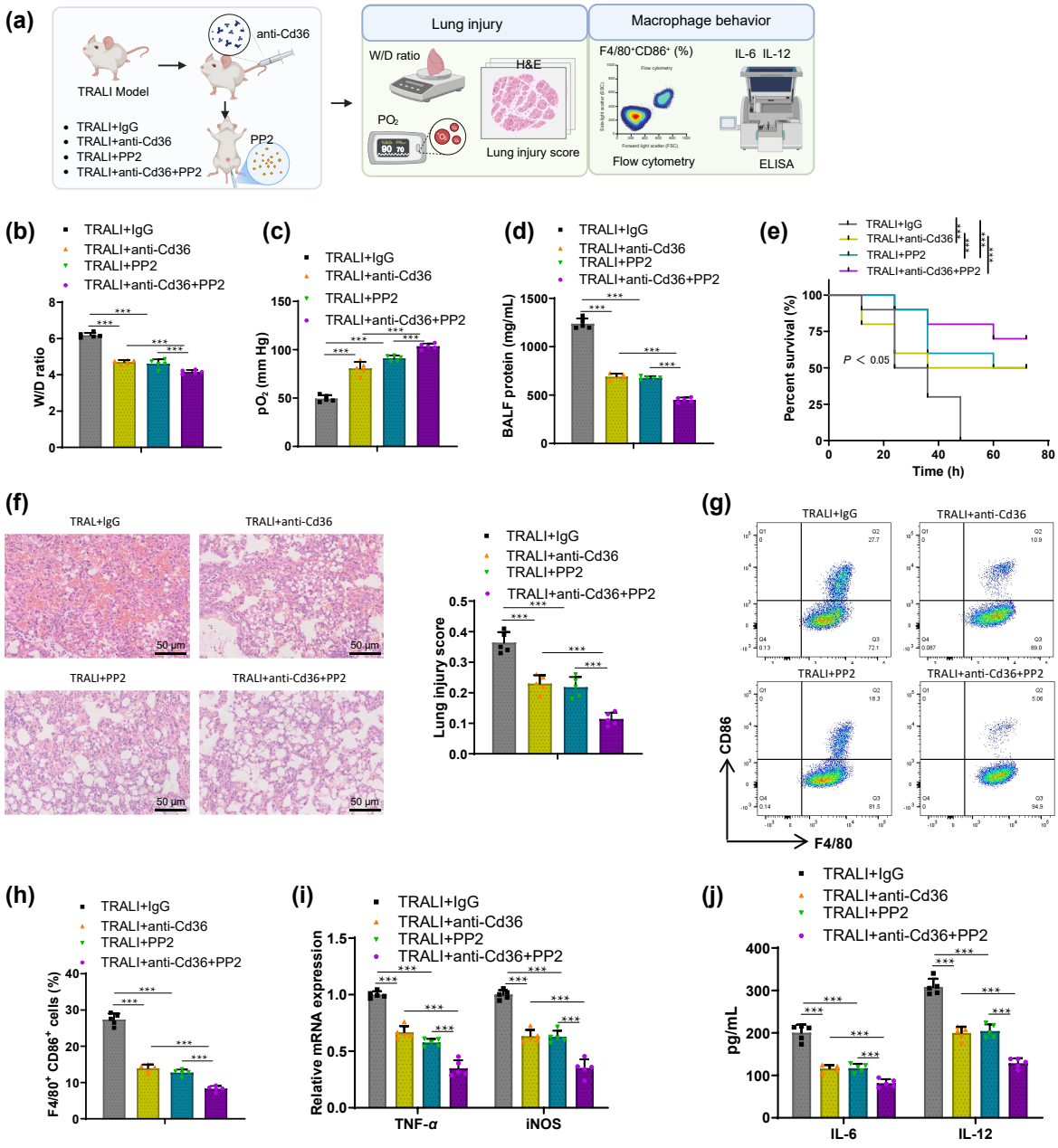

Figure 8 Therapeutic potential of targeting the Cd36-Fyn axis in the TRALI mouse model. (a) Schematic of the experimental workflow for evaluating the therapeutic effect of targeting the Cd36–Fyn axis in TRALI. (b) Lung wet-to-dry weight ratios under different treatment conditions. (c) Measurement of arterial blood PO_2 levels (n = 5). (d) Total protein content in BALF (n = 5). (e) Survival curves of mice under various treatment conditions (n = 10). (f) H&E staining of mouse lung tissue (scale bars = 50 μm) (n = 5). (g) Flow cytometry analysis and (h) quantitative analysis of CD86 expression, an M1 macrophage marker, in lung tissue (n = 5). (i) RT-qPCR analysis of M1 macrophage-related gene expression in lung tissue (n = 5). (j) ELISA quantification of inflammatory cytokines (IL-6 and IL-12) in BALF (n = 5). Data in panels (b)–(d), (f), and (h)–(j) are presented as mean ± SD. The survival curves in panel (e) were analyzed using the log-rank (Mantel–Cox) test. All intergroup comparisons were performed using one-way analysis of variance (ANOVA) followed by Tukey's post hoc multiple-comparison test. $^*P < 0.05$, $^{**}P < 0.01$, $^{***}P < 0.001$.

interferon-gamma (IFN-γ)-activated macrophages can promote macrophage polarization toward an anti-inflammatory M2 phenotype [42]. These observations suggest that the pEVs-induced Cd36–Fyn axis may drive M1 macrophage polarization through these same signaling pathways, which warrants further investigation in future studies.

Notably, existing studies on EV-mediated macrophage polarization have predominantly focused on tumor immune evasion and infectious immune dysregulation. Our study is the first to identify a specific role for pEVs in TRALI-related pulmonary inflammation via the Cd36–Fyn pathway, highlighting the novelty and significance of these findings. Beyond macrophages, dysfunction of neutrophils and pulmonary microvascular endothelial cells has also been implicated in TRALI pathogenesis. Neutrophil-derived reactive oxygen species can directly compromise the pulmonary vascular endothelial barrier [43], while endothelial upregulation of adhesion molecules further exacerbates inflammation and injury [44]. Additionally, metabolic byproducts derived from platelets, such as lysophosphatidylcholine and ceramide, have been shown to aggravate lung injury [45].

Therefore, future research should integrate multiple cell types and metabolic pathways to comprehensively delineate the pathological network underlying TRALI.

In addition, our study provides novel conceptual and translational insights spanning from precise diagnosis to targeted therapy, and identifies potential therapeutic targets for TRALI. Current diagnosis relies largely on clinical exclusion, and specific early laboratory biomarkers remain unavailable. Our findings suggest that circulating pEVs and the expression levels of CD36 on their surface may serve as potential, noninvasive circulating biomarkers. Dynamic post-transfusion monitoring of these parameters may allow early risk assessment before the appearance of overt clinical symptoms and facilitate stratification of patients at increased risk for severe TRALI. From a therapeutic perspective, the CD36–Fyn signaling axis provides a rational framework for targeted intervention. Neutralizing monoclonal antibodies directed against CD36 on the surface of platelet-derived extracellular vesicles could disrupt interactions with pulmonary macrophages and endothelial cells, thereby limiting initiation of downstream inflammatory cascades. Moreover, several Fyn kinase-specific inhibitors, such as Saracatinib (AZD0530), are already undergoing phase II clinical trials for cancer therapy. Repurposing Saracatinib or similar agents for TRALI treatment could substantially shorten development timelines and reduce costs. From the perspective of transfusion medicine, these findings underscore the need to establish quality control standards for the quantity and biological properties of pEVs in stored platelet products and other blood components, enabling the identification and exclusion of "high-risk" blood products and thereby reducing TRALI incidence at the source. In the future, novel processing technologies may be developed to selectively remove or inactivate pathogenic pEVs from blood products while preserving their beneficial functions, ultimately leading to a comprehensive improvement in transfusion safety.

Several limitations of the present study should be acknowledged. First, the TRALI animal model was established through intraperitoneal administration of LPS and pEVs, which offers experimental controllability but does not fully replicate clinical transfusion settings. Future studies will incorporate intravenous tail vein infusion to more closely mimic the clinical onset and progression of TRALI. Second, the pEVs used in this study were derived from PRP without specific validation of platelet origin. In future research, we will adopt more precise isolation techniques, such as magnetic bead sorting or flow cytometry, to ensure purity and specificity. Finally, the role of the Cd36–Fyn pathway was only validated in a murine model, lacking evidence from human clinical samples. Future studies will utilize BALF from TRALI patients and human lung-on-chip models to assess translational relevance and clinical applicability of this pathway. Finally, our study primarily elucidates the critical role of pEVs during the acute inflammatory phase of TRALI. However, accumulating evidence indicates that a substantial proportion of TRALI survivors subsequently develop chronic pulmonary dysfunction, characterized by persistent immune dysregulation, aberrant tissue repair, and progressive pulmonary fibrosis. Accordingly, future studies will further examine the contribution of pEVs to the chronic phase of TRALI by establishing long-term observation models, systematically characterizing longitudinal immune profiles and pulmonary function changes, and determining whether delayed administration of small-molecule inhibitors or neutralizing antibodies targeting the CD36-Fyn axis after resolution of the acute phase can attenuate or prevent progression to chronic pulmonary fibrosis.

This study also suggests that, in addition to the Cd36–Fyn pathway, additional signaling mechanisms and immune cell populations, including monocytes and DCs, may contribute to TRALI pathogenesis. Our single-cell sequencing analysis revealed a significant reduction in the number of monocytes and a decreased proportion of DCs in the TRALI model. Whether these cells are regulated by pEVs and participate in pulmonary inflammation remains an essential question for future investigation. Moreover, the roles of chemokines (e.g., the C-X-C motif chemokine (CXC) family), coagulation factors, and other platelet-derived mediators in TRALI merit further exploration.

This study systematically elucidated the molecular mechanism by which pEVs aggravate TRALI-induced lung injury by activating the Cd36–Fyn signaling axis and promoting M1 macrophage polarization. These findings provide a solid theoretical foundation for advancing our understanding of the immunopathological processes underlying TRALI. Future integration of validation studies using clinical samples with human-derived organ-on-chip platforms may accelerate translation of these mechanistic insights into effective preventive and therapeutic strategies, ultimately improving prognosis and quality of life for patients with TRALI.

5 Conclusions

In this study, we investigated the role of pEVs in TRALI. Using an LPS-primed mouse model, we demonstrated that pEVs markedly aggravated pulmonary inflammation and lung injury, accompanied by increased pro-inflammatory cytokine production and reduced survival. Single-cell RNA sequencing analysis revealed that macrophages were the predominant immune cell population in lung tissue during TRALI. Among the identified macrophage subsets, $Fn1^{+}$ macrophages displayed a pro-inflammatory phenotype and were markedly enriched in the TRALI model, suggesting their involvement in disease progression. Further experiments showed that pEVs promoted macrophage polarization toward the M1 phenotype both *in vitro* and *in vivo*. Mechanistic analyses indicated that Cd36 was highly expressed in macrophages and mediated pEV uptake and macrophage activation. Activation of the downstream Fyn signaling pathway was associated with enhanced inflammatory responses. Importantly, genetic deletion or pharmacological inhibition of Cd36 or Fyn attenuated macrophage inflammatory activation, alleviated lung injury, and improved survival in the TRALI mouse model. Taken together, these findings demonstrate that platelet-derived extracellular vesicles promote TRALI progression by inducing M1 macrophage polarization through the Cd36–Fyn signaling pathway, highlighting this signaling axis as a key mechanism underlying pEV-mediated inflammatory lung injury.

Electronic Supplementary Material: Supplementary material (additional experimental data and methodological details supporting the main findings, including characterization of pEVs and platelet storage–related parameters (Fig. S1), quality control and data processing for single-cell RNA sequencing (scRNA-seq) analysis (Fig. S2), macrophage subpopulation trajectory analysis and gene expression dynamics (Fig. S3), differential gene expression analysis and candidate gene identification related to TRALI progression (Fig. S4), validation of Cd36 knockdown and antibody

inhibition experiments (Fig. S5), and additional *in vivo* experimental data related to Cd36 and Fyn deficiency in the TRALI mouse model (Fig. S6), detailed information on antibodies, shRNA sequences, and RT-qPCR primers is listed in Tables S1–S3, and complete differential gene datasets are provided in Tables S4–S6) is available in the online version of this article at https://doi.org/10.26599/NR.2026.94908388.

Data Availability

All data generated or analyzed during this study are included in this article and/or its supplementary material files. Further inquiries can be directed to the corresponding author.

Acknowledgments

This study was supported by Natural Science Foundation Program of Jiangxi Province (Nos. 20232BAB216040 and 20252BAC240526), the National Natural Science Foundation of China (Nos. 82560048 and 82472225), Science and Technique Point Program of Department of Education of Jiangxi Province (No. GJJ210112), and Science and technology innovation base plan of Jiangxi Province-Key Laboratory of Jiangxi Province for Transfusion Medicine (No. 2024SSY06171).

Declaration of competing interest

All the contributing authors report no conflict of interests in this work.

Author contribution statement

C. G. W, and J. M. H. contributed equally to this work. C. G. W, and J. M. H. designed and performed the experiments, analyzed data, and drafted the manuscript. W. L., L. J. K., and Y. Z. W. assisted with experimental procedures, data collection, and interpretation. A. P. L. conceived and supervised the study, acquired funding, and critically revised the manuscript. All authors read and approved the final version of the manuscript.

Informed consent

Not applicable.

Ethics statement

The animal study protocol was approved by the Institutional Animal Care and Use Committee at The First Affiliated Hospital of Nanchang University (Ethics code: CDYFY-IACUC-202404QR028).

Use of AI statement

None.

References

[1] Ackfeld, T.; Schmutz, T.; Guechi, Y.; Le Terrier, C. Blood transfusion reactions—a comprehensive review of the literature including a Swiss Perspective. *J. Clin. Med.* **2022**, *11*, 2859.

[2] Hu, L. Y.; Wang, B. L.; Jiang, Y.; Zhu, B. H.; Wang, C.; Yu, Q.; Hou, W. J.; Xia, Z. F.; Wu, G. S.; Sun, Y. Risk factors for transfusion-related acute lung injury. *Respir. Care* **2021**, *66*, 1029–1038.

[3] Iyer, M. H.; Kumar, J. E.; Kumar, N.; Gorelik, L.; Hussain, N.; Stein, E.; Bhatt, A. M.; Bhandary, S.; Essandoh, M. K.; Flores, A. S. Transfusion-related acute lung injury during liver transplantation: A scoping review. *J. Cardiothorac. Vasc. Anesth.* **2022**, *36*, 2606–2615.

[4] Huang, M. G. T. Y.; Wang, X. T.; Wang, L.; Chen, G. Y. Transfusion-Related acute lung injury (TRALI) caused by antibodies to HLA-DRB1* 07:01 and HLA-DQB1*02:02: A case report. *Clin. Case Rep.* **2023**, *11*, e8284.

[5] Perez-Viloria, M. E.; Lopez, K.; Malik, F.; Yatham, P.; Lopez, O.; Oh, K. S.; Alghamdi, S.; Garcia, G. Transfusion-related acute lung injury (TRALI) in postoperative anesthesia care unit (PACU) after one unit of platelets: A case report. *Cureus* **2022**, *14*, e29274.

[6] McVey, M. J.; Weidenfeld, S.; Maishan, M.; Spring, C.; Kim, M.; Tabuchi, A.; Srbely, V.; Takabe-French, A.; Simmons, S.; Arenz, C. et al. M. Platelet extracellular vesicles mediate transfusion-related acute lung injury by imbalancing the sphingolipid rheostat. *Blood* **2021**, *137*, 690–701.

[7] Popovsky, M. A.; Abel, M. D.; Moore, S. B. Transfusion-related acute lung injury associated with passive transfer of antileukocyte antibodies. *Am. Rev. Respir. Dis.* **1983**, *128*, 185–189.

[8] Peters, A. L.; van Hezel, M. E.; Juffermans, N. P.; Vlaar, A. P. J. Pathogenesis of non-antibody mediated transfusion-related acute lung injury from bench to bedside. *Blood Rev.* **2015**, *29*, 51–61.

[9] Yu, Y. H.; Lian, Z. Q. Update on transfusion-related acute lung injury: An overview of its pathogenesis and management. *Front. Immunol.* **2023**, *14*, 1175387.

[10] van Niel, G.; Carter, D. R. F.; Clayton, A.; Lambert, D. W.; Raposo, G.; Vader, P. Challenges and directions in studying cell-cell communication by extracellular vesicles. *Nat. Rev. Mol. Cell Biol.* **2022**, *23*, 369–382.

[11] Gupta, D.; Zickler, A. M.; El Andaloussi, S. Dosing extracellular vesicles. *Adv. Drug Deliv. Rev.* **2021**, *178*, 113961.

[12] O'Brien, K.; Breyne, K.; Ughetto, S.; Laurent, L. C.; Breakefield, X. O. RNA delivery by extracellular vesicles in mammalian cells and its applications. *Nat. Rev. Mol. Cell Biol.* **2020**, *21*, 585–606.

[13] Goubran, H.; Seghatchian, J.; Sabry, W.; Ragab, G.; Burnouf, T. Platelet and extracellular vesicles in COVID-19 infection and its vaccines. *Transfus. Apher. Sci.* **2022**, *61*, 103459.

[14] Obeid, S.; Sung, P. S.; Le Roy de Boiseaumarie Engineer, B.; Chou, M. L.; Hsieh, S. L.; Elie-Caille, C.; Burnouf, T.; Boireau, W. NanoBioAnalytical characterization of extracellular vesicles in 75-nm nanofiltered human plasma for transfusion: A tool to improve transfusion safety. *Nanomedicine* **2019**, *20*, 101977.

[15] van der Laan, Z.; Eveline, A. N.; van der Velden, S.; Porcelijn, L.; Semple, J. W.; van der Schoot, C. E.; Kapur, R. Update on the pathophysiology of transfusion-related acute lung injury. *Curr. Opin. Hematol.* **2020**, *27*, 386–391.

[16] Chen, Y. N.; Hu, M. R.; Wang, L.; Chen, W. D. Macrophage M1/M2 polarization. *Eur. J. Pharmacol.* **2020**, *877*, 173090.

[17] Hu, Q.; Lyon, C. J.; Fletcher, J. K.; Tang, W. F.; Wan, M. H.; Hu, T. Y. Extracellular vesicle activities regulating macrophage- and tissue-mediated injury and repair responses. *Acta Pharm. Sin. B* **2021**, *11*, 1493–1512.

[18] Xiao, Y.; Peng, X. X.; Peng, Y.; Zhang, C.; Liu, W.; Yang, W. J.; Dou, X. W.; Jiang, Y. Y.; Wang, Y. X.; Yang, S. et al. Macrophage - derived extracellular vesicles regulate follicular activation and improve ovarian function in old mice by modulating local environment. *Clin. Transl. Med.* **2022**, *12*, e1071.

[19] Song, N.; Pan, K. F.; Chen, L.; Jin, K. K. Platelet derived vesicles enhance the TGF-beta signaling pathway of M1 macrophage. *Front. Endocrinol.* **2022**, *13*, 868893.

[20] Shu, H. Y.; Peng, Y. Z.; Hang, W. J.; Nie, J. L.; Zhou, N.; Wang, D. W. The role of CD36 in cardiovascular disease. *Cardiovasc. Res.* **2020**, *118*, 115–129.

[21] Jay, A. G.; Chen, A. N.; Paz, M. A.; Hung, J. P.; Hamilton, J. A. CD36 binds oxidized low density lipoprotein (LDL) in a mechanism

dependent upon fatty acid binding. *J. Biol. Chem.* **2015**, *290*, 4590–4603.
[22] Zhu, W. F.; Li, W.; Silverstein, R. L. Advanced glycation end products induce a prothrombotic phenotype in mice via interaction with platelet CD36. *Blood* **2012**, *119*, 6136–6144.
[23] Zhao, L.; Zhang, C.; Luo, X. X.; Wang, P.; Zhou, W.; Zhong, S.; Xie, Y. X.; Jiang, Y. B.; Yang, P.; Tang, R. K. et al. CD36 palmitoylation disrupts free fatty acid metabolism and promotes tissue inflammation in non-alcoholic steatohepatitis. *J. Hepatol.* **2018**, *69*, 705–717
[24] Aslam, R.; Speck, E. R.; Kim, M.; Freedman, J.; Semple, J. W. Transfusion‐related immunomodulation by platelets is dependent on their expression of MHC Class I molecules and is independent of white cells. *Transfusion* **2008**, *48*, 1778–1786.
[25] Chen, F.; Dai, X. Q.; Li, A. Z.; Zheng, Y. H.; Hu, W. Quality assessment of the preparation and storage of leukocyte-depleted pooled platelet concentrates. *Hematology* **2024**, *29*, 2293492.
[26] Chen, H. C.; Chien, W. C.; Chang, M. Y.; Hsieh, M. Y.; Lai, M. D.; Maa, M. C.; Leu, T. H. The iNOS/Src/FAK axis contributes to lithium chloride-mediated macrophage migration. *Nitric Oxide* **2015**, *47*, 58–64.
[27] Wen, C.; Seeger, R. C.; Fabbri, M.; Wang, L.; Wayne, A. S.; Jong, A. Y. Biological roles and potential applications of immune cell‐derived extracellular vesicles. *J. Extracell. Vesicles* **2017**, *6*, 1400370.
[28] Chen, Y. L.; Yang, M. A.; Huang, W. X.; Chen, W. J.; Zhao, Y. Q.; Schulte, M. L.; Volberding, P.; Gerbec, Z.; Zimmermann, M. T.; Zeighami, A. et al. Mitochondrial metabolic reprogramming by CD36 signaling drives macrophage inflammatory responses. *Circ. Res.* **2019**, *125*, 1087–1102.
[29] Laursen, L. S.; Chan, C. W.; ffrench-Constant, C. An integrin-contactin complex regulates CNS myelination by differential Fyn phosphorylation. *J. Neurosci.* **2009**, *29*, 9174–9185.
[30] Nguyen, T. H.; Liu, J.; Lombroso, P. J. Striatal enriched phosphatase 61 dephosphorylates Fyn at phosphotyrosine 420. *J. Biol. Chem.* **2002**, *277*, 24274–24279.
[31] Juffermans, N. P.; Aubron, C.; Duranteau, J.; Vlaar, A. P. J.; Kor, D. J.; Muszynski, J. A.; Spinella, P. C.; Vincent, J. L. Transfusion in the mechanically ventilated patient. *Intensive Care Med.* **2020**, *46*, 2450–2457.
[32] van den Akker, T. A.; Grimes, Z. M.; Friedman, M. T. Transfusion-associated circulatory overload and transfusion-related acute lung injury: A review of underreported entities with current updates. *Am. J. Clin. Pathol.* **2021**, *156*, 529–539.
[33] Tung, J. P.; Chiaretti, S.; Dean, M. M.; Sultana, A. J.; Reade, M. C.; Fung, Y. L. Transfusion-related acute lung injury (TRALI): Potential pathways of development, strategies for prevention and treatment, and future research directions. *Blood Rev.* **2022**, *53*, 100926.
[34] Mandel, J.; Casari, M.; Stepanyan, M.; Martyanov, A.; Deppermann, C. Beyond hemostasis: Platelet innate immune interactions and thromboinflammation. *Int. J. Mol. Sci.* **2022**, *23*, 3868.
[35] Song, D. Y.; Adrover, J. M.; Felice, C.; Christensen, L. N.; He, X. Y.; Merrill, J. R.; Wilkinson, J. E.; Janowitz, T.; Lyons, S. K.; Egeblad, M. et al. PTP1B inhibitors protect against acute lung injury and regulate CXCR4 signaling in neutrophils. *JCI Insight* **2022**, *7*, 158199
[36] Silliman, C. C.; Boshkov, L. K.; Mehdizadehkashi, Z.; Elzi, D. J.; Dickey, W. O.; Podlosky, L.; Clarke, G.; Ambruso, D. R. Transfusion-related acute lung injury: Epidemiology and a prospective analysis of etiologic factors. *Blood* **2003**, *101*, 454–462.
[37] Menis, M.; Anderson, S. A.; Forshee, R. A.; McKean, S.; Johnson, C.; Warnock, R.; Gondalia, R.; Mintz, P. D.; Holness, L.; Worrall, C. M. et al. Transfusion‐related acute lung injury and potential risk factors among the inpatient US elderly as recorded in Medicare claims data, during 2007 through 2011. *Transfusion* **2014**, *54*, 2182–2193.
[38] Klanderman, R. B.; van Mourik, N.; Eggermont, D.; Peters, A. L.; Tuinman, P. R.; Bosman, R.; Endeman, H.; Cremer, O. L.; Arbous, S. M.; Vlaar, A. P. J. Incidence of transfusion‐related acute lung injury temporally associated with solvent/detergent plasma use in the ICU: A retrospective before and after implementation study. *Transfusion* **2022**, *62*, 1752–1762.
[39] Marotta, G.; Basagni, F.; Rosini, M.; Minarini, A. Role of Fyn kinase inhibitors in switching neuroinflammatory pathways. *Curr. Med. Chem.* **2022**, *29*, 4738–4755.
[40] Maaninka, K.; Neuvonen, M.; Kerkelä, E.; Hyvärinen, K.; Palviainen, M.; Kamali-Moghaddam, M.; Federico, A.; Greco, D.; Laitinen, S.; Öörni, K. et al. OxLDL sensitizes platelets for increased formation of extracellular vesicles capable of finetuning macrophage gene expression. *Eur. J. Cell Biol.* **2023**, *102*, 151311.
[41] Holz, K.; Prinz, M.; Brendecke, S. M.; Hölscher, A.; Deng, F. Y.; Mitrücker, H. W.; Rose-John, S.; Hölscher, C. Differing outcome of experimental autoimmune encephalitis in macrophage/neutrophil- and T cell-specific gp130-deficient mice. *Front. Immunol.* **2018**, *9*, 836.
[42] Ma, Y. M.; Meng, F. Q.; Lin, Z. D.; Chen, Y. J.; Lan, T. Y.; Yang, Z. X.; Diao, R.; Zhang, X. Z.; Chen, Q.; Zhang, C. et al. Bioengineering platelets presenting PD‐L1, galectin‐9 and BTLA to ameliorate type 1 diabetes. *Adv. Sci.* **2025**, *12*, e2501139.
[43] Strait, R. T.; Hicks, W.; Barasa, N.; Mahler, A.; Khodoun, M.; Köhl, J.; Stringer, K.; Witte, D.; van Rooijen, N.; Susskind, B. M. et al. MHC class I-specific antibody binding to nonhematopoietic cells drives complement activation to induce transfusion-related acute lung injury in mice. *J. Exp. Med.* **2011**, *208*, 2525–2544.
[44] Morsing, K. S. H.; Peters, A. L.; van Buul, J. D.; Vlaar, A. P. J. The role of endothelium in the onset of antibody-mediated TRALI. *Blood Rev.* **2018**, *32*, 1–7.
[45] Zeeuw van der Laan, E. A. N.; van der Velden, S.; Porcelijn, L.; Semple, J. W.; van der Schoot, C. E.; Kapur, R. Evaluation of platelet responses in transfusion-related acute lung injury (TRALI). *Transfus. Med. Rev.* **2020**, *34*, 227–233.